J. Fluid Mech. (2002), *vol.* 458, *pp.* 103–132.
DOI: 10.1017/S0022112002007826 Printed in the United Kingdom

Study on the spin-up of fluid in a rectangular container using Ekman pumping models

By Y. K. SUH AND Y. H. CHOI

Department of Mechanical Engineering, Dong-A University, Pusan 604-714, Korea

(Received 25 June 2001 and in revised form 25 October 2001)

Spin-up in a rectangular container with a free surface is investigated numerically and experimentally. In the formulation of two-dimensional numerical computation, we use a potential-like function in addition to the stream function to deal with the first-order Ekman pumping model. It is shown that our numerical results are in good agreement with those obtained by the experiment when either the leading-order or first-order pumping model is used. On the other hand, when no pumping effect is considered the numerical results show, except in the initial development, a considerable discrepancy from those of the experiment. Our attention in this study is focused on clarifying the physical mechanism of cyclonic vortex merging. At low Reynolds numbers and/or liquid depths the Ekman pumping damps the vortical flows fast, resulting in non-merging. At moderate Reynolds numbers, it enhances merging because the cyclonic vortices expand due to the Ekman pumping. We discuss the influence of various parameters, including Reynolds number, Rossby number, and dimensionless liquid depth, on the evolution of the vortical flows.

1. Introduction

Spin-up flow has applications in a broad range of areas such as turbomachinery, the motion of liquid fuel within space craft, oceanic flow, and mantle movement inside the Earth. Up to about 1990, most of the studies on the subject concerned axisymmetric containers. In this configuration spin-up flow is dominated by the secondary motion (called Ekman circulation) caused by Ekman pumping and defined on the meridional plane. From about 1990 however non-axisymmetric configurations have attracted fluid dynamicists' attention, and it has been shown that the Ekman circulation is preceded by two-dimensional separation from the lateral wall surfaces and the subsequent development of interesting vortical flows. Once several vortices are established inside the container they interact not only with each other but also with the sidewalls. Thus, aside from its intrinsic importance, the spin-up in non-axisymmetric containers can give further insight into various geophysical flow phenomena.

Van Heijst (1989) presented experimental evidence of two-dimensional separation and the subsequent evolution of vortical flows leading to a self-organized cell structure inside non-axisymmetric cylinders of various shapes built by combining circular cylinders and flat plates.

Spin-up in rectangular containers was first studied experimentally by van Heijst, Davies & Davis (1990) at Reynolds number $O(10^5)$. This geometry, albeit simple, turned out to provide rich phenomena. They discerned three main stages in the spin-up process: (i) the starting flow, characterized by a uniform relative vorticity, (ii) flow separation from the lateral walls, and (iii) subsequent organization of vortical

flows into a regular array. Merging of a pair of cyclonic vortices originating from separate corners occurs in the third stage, and van Heijst *et al.* (1990) attributed this phenomenon to the free-surface deformation. (But later this argument had to be supplemented by the lateral wall effect, i.e. image vortex, van de Konijnenberg & van Heijst 1997.) They also observed a critical situation at which, depending on a small unknown disturbance, the central dumbbell-shape vortex (anticyclonic) either split into two, leading to the cyclones merging, or reorganized into a regular cell resulting in non-merging. Suh (1994) has numerically shown that purely two-dimensional Navier–Stokes equations can predict well the early development of the spin-up flow, and he has also reproduced the critical phenomena by modulating an artificial initial condition composed of a cyclonic–anticyclonic–cyclonic cell arrangement. However, in most of his numerical results for the actual spin-up flow, the merging did not take place.

Henderson, Lopez & Stewart (1996) studied the same flow problem using both experimental and numerical methods. They stressed that there exists a critical Reynolds number below which no merging is expected, as was the case found by Suh (1994). They also asserted that Ekman pumping is not required for the vortex merging, as evidenced by their two-dimensional numerical computation without a pumping model. However the numerical merging begins at a time 2.5 times later than observed in the experiment. Further experimental study by the van Heijst group (van de Konijnenberg & van Heijst 1997) on the rectangular tank has focused on the effect of the free-surface deformation on, in particular, the merging phenomena. Here, it is concluded that the free-surface deformation is a discouraging factor for the merging, contrary to their early conjecture (van Heijst *et al.* 1990).

Common conclusions obtained by these investigations can be summarized as follows. (i) Although turbulence may exist at the very initial point of the spin-up process, it soon decays, and the following early stage including the separation from lateral walls and cyclonic vortex formation is essentially a two-dimensional phenomenon. (ii) Merging of cyclones does not occur at low Reynolds numbers, say $O(10^3)$. At higher Reynolds numbers, $O(10^4)$, merging is expected more often than not. (iii) There exists a critical horizontal aspect ratio of the tank beyond which no merging is observed, and it depends on other parameters, such as Reynolds number. (iv) The effect of liquid depth is not monotonical. For instance, Henderson *et al.* (1996) observed that when the liquid depth is increased the critical Reynolds number on the whole decreases at first and then increases sharply. (v) At much higher Reynolds number, say $O(10^5)$, the cellular pattern tends to be asymmetric, and vortex evolution becomes far more complex.

However some fundamental questions are not answered yet. (i) What is the basic mechanism of the vortex merging? (ii) What is the role of Ekman pumping? (iii) To what extent will the free-surface deformation influence the merging?

In this study we focus on the role of the Ekman pumping in the spin-up of rectangular containers, and we aim to answer some of the above questions, specifically (i) and (ii). For this purpose, we use both numerical and experimental methods. Up to now, no successful comparison has been reported between the two results, except for low Reynolds numbers and at the very beginning of the spin-up process. Further, three-dimensional computation still demands a high cost. Thus, we develop a two-dimensional numerical model which encompasses not only the leading-order but also the first-order Ekman model. Zavala Sansón & van Heijst (2000) have already applied the leading-order model to their two-dimensional computation for the axisymmetric problems, showing that significant improvement can be established by taking the

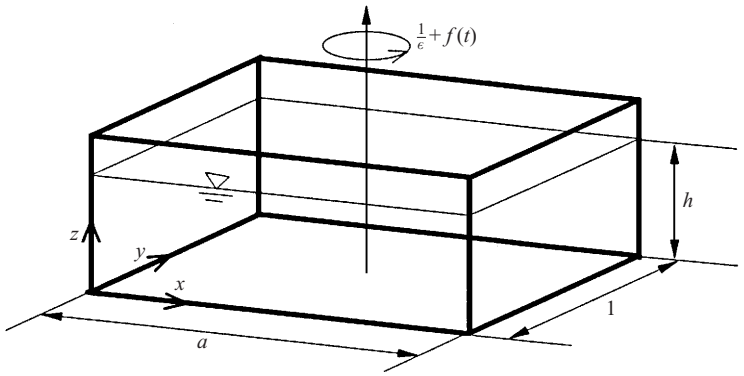

FIGURE 1. Schematic view of a homogeneous fluid contained in a rectangular tank, and dimensionless coordinates.

Ekman model into consideration. However no results have been reported for the non-axisymmetric cases in which a variety of interesting flow phenomena such as two-dimensional boundary-layer separation and vortex merging/splitting occur.

This paper is organized as follows. In the following section, a two-dimensional numerical model is derived which includes the Ekman pumping laws. The numerical method is also explained in this section. In § 3, the experimental apparatus and the PIV method are briefly described. We present and discuss the results in § 4, which is followed by a summary and conclusions in § 5.

2. Formulation and numerical method

We consider a fluid of viscosity ν and density ρ contained in a rectangular tank of length L and width B in a depth H with a free surface (refer to figure 1 which shows the tank configuration in dimensionless quantities). The tank is initially rotating about the central vertical axis at a constant angular velocity Ω_s and the fluid is in a state of solid-body rotation. The rotational speed of the system is then increased smoothly and finally kept constant at a new speed $\Omega_f = \Omega_s + \Delta\Omega$. The spin-up flow arising during and after this change is basically horizontal and depth-independent under the asymptotic restriction $\Delta\Omega \ll \Omega_f$ (Taylor–Proudman theorem). (This still holds even if the whole system is arbitrarily tilted as long as the container is completely closed without a free surface.) Thus, some two-dimensional phenomena occurring in the early stage of the spin-up process, such as separation from lateral walls, can be captured by purely two-dimensional Navier–Stokes equations, as shown by Suh (1994) and Henderson *et al.* (1996). However the numerical results could not satisfactorily predict the later stage; for instance, Henderson *et al.* (1996) numerically reproduced the merging event at $Re = 10000$ for the aspect ratio 2.2, but the event began to occur at a time 2.5 times later than the experiment. We postulate that the Ekman pumping from the bottom wall may play a significant role in the later stage of the process. To account for the pumping effect in the formulation, we divide the region into two: the upper layer, which occupies most of the tank and is governed by two-dimensional equations; and the lower layer, which is very thin; for this, the boundary-layer approximation can be applicable but the flow field should be three-dimensional.

2.1. *Upper layer; vorticity equation*

Taking B, $\Delta\Omega^{-1}$, $B\Delta\Omega$ and $\rho B^2\Omega_f\Delta\Omega$ as the reference length, time, velocity and pressure, respectively, we can write the governing equations in dimensionless form as follows:

$$\frac{\partial u}{\partial t}+u\frac{\partial u}{\partial x}+v\frac{\partial u}{\partial y}-2\left[\frac{1}{\epsilon}+f(t)\right]v=-\frac{1}{\epsilon}\frac{\partial p}{\partial x}+\frac{1}{Re}\nabla^2 u+y\frac{\mathrm{d}f}{\mathrm{d}t}, \tag{2.1}$$

$$\frac{\partial v}{\partial t}+u\frac{\partial v}{\partial x}+v\frac{\partial v}{\partial y}+2\left[\frac{1}{\epsilon}+f(t)\right]u=-\frac{1}{\epsilon}\frac{\partial p}{\partial y}+\frac{1}{Re}\nabla^2 v-x\frac{\mathrm{d}f}{\mathrm{d}t}, \tag{2.2}$$

$$\frac{\partial u}{\partial x}+\frac{\partial v}{\partial y}+\frac{\partial w}{\partial z}=0 \tag{2.3}$$

where the coordinates x, y and z are attached to the container as shown in figure 1, and two-dimensionality is assumed for the horizontal velocity components and the pressure; $u=u(x,y,t)$, $v=v(x,y,t)$, $p=p(x,y,t)$. For the vertical velocity component w, a linear profile in the vertical distribution will be assumed, as will be discussed shortly. The centrifugal and gravitational forces are absorbed in p. The function $f(t)$ denotes the non-dimensional difference of the instant angular speed of the container from the final value; in this study f is defined as

$$f(t)=\begin{cases}-\frac{1}{2}(1+\cos\omega t), & 0\leqslant t\leqslant t_s\\ 0, & t\geqslant t_s,\end{cases} \tag{2.4}$$

for a smooth speed-up operation in the experiment, where $t_s=\pi/\omega$ is the non-dimensional speed-up time.

Parameters involved in the model are

$$Re=\frac{B^2\Delta\Omega}{\nu},\quad \epsilon=\frac{\Delta\Omega}{\Omega_f},\quad a=\frac{L}{B},\quad h=\frac{H}{B}. \tag{2.5}$$

Here Re is the Reynolds number, ϵ the Rossby number, a the aspect ratio, and h the dimensionless liquid depth. For the flow depth-independence, it is required that $Re\gg 1$ and $\epsilon\ll 1$; however, as will be shown in § 4, the numerical results with even moderate values of ϵ are in good agreement with the experimental results (see also Zavala Sansón & van Heijst 2000).

To close the problem, the vertical velocity component w appearing in (2.3) must be specified. As can be seen from (2.3), for the two-dimensional model to be valid, w must be a linear function of z:

$$w=\left(1-\frac{z}{h}\right)w_E, \tag{2.6}$$

where $w_E(x,y,t)$ is the Ekman pumping velocity induced by the friction at the bottom wall. In this study, we neglect the free-surface deformation. Then the continuity equation (2.3) becomes

$$\frac{\partial u}{\partial x}+\frac{\partial v}{\partial y}=\frac{w_E}{h}. \tag{2.7}$$

The analysis of the Ekman boundary layer flows supplies w_E in relation with the upper-layer variables as shown in § 2.2.

As usual, we introduce the vorticity

$$\zeta=\frac{\partial v}{\partial x}-\frac{\partial u}{\partial y}, \tag{2.8}$$

and eliminate the pressure gradients from (2.1) and (2.2) to obtain the vorticity equation:

$$\frac{\partial \zeta}{\partial t} + u\frac{\partial \zeta}{\partial x} + v\frac{\partial \zeta}{\partial y} = -\frac{w_E}{h}\left(\frac{2}{\epsilon} + \zeta + 2f\right) + \frac{1}{Re}\nabla^2\zeta - 2\frac{\mathrm{d}f}{\mathrm{d}t}. \tag{2.9}$$

Boundary conditions are simply

$$u = v = 0 \quad \text{on} \quad x = 0,\ a \quad \text{and} \quad y = 0,\ 1, \tag{2.10}$$

which guarantees both the impermeable and no-slip conditions.

In summary, the vorticity is determined by (2.9), and velocity components by (2.7) and (2.8) with ζ and w_E being specified.

2.2. *Lower layer; Ekman pumping models*

To analyse the bottom layer flows, we use two strained variables Z and W defined as

$$Z = z/\sqrt{E}, \quad W = w/\sqrt{E},$$

where $E = \epsilon/Re = (B^2\Omega_f/\nu)^{-1}$ is the Ekman number based on the reference length B (not on the depth H). Note that E here is just used for simplicity of the formulation, not as an independent parameter, and $E \ll 1$ is naturally assumed. Using the classical boundary-layer approximation, we can write the momentum and continuity equations as follows:

$$\frac{\partial^2 Q}{\partial Z^2} - 2\mathrm{i}(Q-q) = \epsilon\left[\frac{\partial}{\partial t}(Q-q) + 2\mathrm{i}f(Q-q) - \frac{1}{Re}\nabla^2(Q-q) + U\frac{\partial Q}{\partial x} + V\frac{\partial Q}{\partial y} + W\frac{\partial Q}{\partial Z} - u\frac{\partial q}{\partial x} - v\frac{\partial q}{\partial y}\right], \tag{2.11}$$

$$\frac{\partial U}{\partial x} + \frac{\partial V}{\partial y} + \frac{\partial W}{\partial Z} = 0, \tag{2.12}$$

where $Q = U + \mathrm{i}V$ and $q = u + \mathrm{i}v$ are complex velocities defined in the lower and upper layers, respectively. Note that the horizontal viscous term $\nabla^2(Q-q)/Re$ is retained on the right-hand side of (2.11), since it does not add complexity in the analysis.

The boundary conditions are

$$Q = W = 0 \quad \text{on} \quad Z = 0, \quad (Q, W) \to (q, w) \quad \text{as} \quad Z \to \infty. \tag{2.13a,b}$$

The Ekman pumping velocity in terms of W is given by

$$W_E = -\int_0^\infty \left(\frac{\partial U}{\partial x} + \frac{\partial V}{\partial y}\right)\mathrm{d}Z. \tag{2.14}$$

Solving (2.11) and (2.12) for Q and W numerically may require enormous computer time and is not consistent with our primary purpose. Instead, taking ϵ as a small parameter, we use a regular perturbation method to derive a relationship between w_E and the upper-layer variables. Thus, we expand Q and W like

$$(Q, W) = (Q_0, W_0) + \epsilon(Q_1, W_1) + \cdots,$$

substitute into (2.11), equate terms of equal power of ϵ, and then obtain

$$\frac{\partial^2 Q_0}{\partial Z^2} - 2\mathrm{i}Q_0 = -2\mathrm{i}q, \tag{2.15}$$

$$\frac{\partial^2 Q_1}{\partial Z^2} - 2\mathrm{i}Q_1 = \frac{\partial}{\partial t}(Q_0 - q) + 2\mathrm{i}f(Q_0 - q) - \frac{1}{Re}\nabla^2(Q_0 - q) + U_0\frac{\partial Q_0}{\partial x} + V_0\frac{\partial Q_0}{\partial y} + W_0\frac{\partial Q_0}{\partial Z} - u\frac{\partial q}{\partial x} - v\frac{\partial q}{\partial y}, \quad (2.16)$$

etc. The Ekman pumping velocity is given by

$$w_E = w_{E0} + \epsilon w_{E1} + \cdots, \quad (2.17)$$

and our target is to relate the first two terms with the upper-layer variables.

Solution of the leading-order equation (2.15) is well known:

$$Q_0 = q[1 - \mathrm{e}^{-(1+\mathrm{i})Z}]. \quad (2.18)$$

W_0 is obtained from (2.12):

$$W_0 = \frac{\zeta}{4}\left[2 - (1+\mathrm{i})\mathrm{e}^{-(1+\mathrm{i})Z} - (1-\mathrm{i})\mathrm{e}^{-(1-\mathrm{i})Z}\right] + \frac{w_E}{4h}\left[2 - (1-\mathrm{i})\mathrm{e}^{-(1+\mathrm{i})Z} - (1+\mathrm{i})\mathrm{e}^{-(1-\mathrm{i})Z}\right] - \frac{w_E}{h}Z. \quad (2.19)$$

The last term in the right-hand side of (2.19) is to be matched with the corresponding one in (2.6). Taking $E \to 0$ and $Z \to \infty$, we obtain from (2.19) the well-known linear Ekman pumping law:

$$w_{E0} = \frac{\sqrt{E}}{2}\zeta. \quad (2.20)$$

Substituting (2.18) and (2.19) into the right-hand side of (2.16) and solving for Q_1 gives w_{E1}. After some tedious algebraic work, we end up with

$$w_{E1} = -\sqrt{E}\left[-\frac{1}{4}\frac{\mathrm{d}f}{\mathrm{d}t} + \frac{1}{4}f\zeta + \frac{7}{80}\zeta^2 + \frac{3}{80}\left(u\frac{\partial\zeta}{\partial x} + v\frac{\partial\zeta}{\partial y}\right) + \frac{7}{80}\left(-u\frac{\partial\zeta}{\partial y} + v\frac{\partial\zeta}{\partial x}\right) + \frac{3}{20}\left(\frac{\partial u}{\partial y}\frac{\partial v}{\partial x} - \frac{\partial u}{\partial x}\frac{\partial v}{\partial y}\right)\right]. \quad (2.21)$$

In the above formula $\partial\zeta/\partial t - \nabla^2\zeta/Re$ has been replaced by $-(u\partial\zeta/\partial x + v\partial\zeta/\partial y + 2\mathrm{d}f/\mathrm{d}t)$ for convenience in the numerical work; this identity comes from (2.9) with the divergence $(\partial u/\partial x + \partial v/\partial y)$ neglected. The formula (2.21) is in essence identical with that derived by Hart (1995, 2000).

2.3. *Equations for velocities*

To solve (2.7) and (2.8) for u and v, we introduce ψ and ϕ defined as

$$u = \frac{\partial\psi}{\partial y} + \frac{\partial\phi}{\partial x}, \quad v = -\frac{\partial\psi}{\partial x} + \frac{\partial\phi}{\partial y}. \quad (2.22a,b)$$

Substitution of these into (2.8) and (2.7) results in

$$\nabla^2\psi = -\zeta, \quad \nabla^2\phi = \frac{w_E}{h}. \quad (2.23a,b)$$

In the leading-order Ekman pumping model, w_E is proportional to ζ, (2.20), and this leads to

$$\phi = -\frac{\sqrt{E}}{2h}\psi. \quad (2.24)$$

Thus, in this case it is sufficient to solve only (2.23a), as done by Zavala Sansòn

& van Heijst (2000). For the first-order Ekman pumping model, however, a simple relationship between w_E and ζ no longer exists, and the two equations (2.23a, b) must be solved independently.

Boundary conditions should reflect the impermeable restriction on each wall:

$$\psi = 0 \quad \text{on} \quad x = 0, a \quad \text{and} \quad y = 0, 1, \tag{2.25}$$

$$\frac{\partial \phi}{\partial n} = 0 \quad \text{on} \quad x = 0, a \quad \text{and} \quad y = 0, 1, \tag{2.26}$$

where n denotes the coordinate normal to each lateral wall. On the other hand no-slip conditions are applied in solving the vorticity equation (2.9), and will be described in § 2.5.

We remark that ψ and ϕ can be called stream and potential functions respectively, but only in an asymptotical sense for small E.

2.4. *Role of the Ekman effects*

In understanding the role of the Ekman effects, the relationship between the pumping velocity and the vorticity of the upper layer is prerequisite for a clearer picture, and we employ a linear relation (2.20) for this purpose. In the following analysis, we call the vortex with $\zeta > 0$ cyclonic and that with $\zeta < 0$ anticyclonic. Thus the cyclonic and anticyclonic vortices give Ekman pumping ($w_E > 0$) and suction ($w_E < 0$), respectively. We also assume $f = 0$.

Then the vorticity equation (2.9) reads

$$\frac{\partial \zeta}{\partial t} + \boldsymbol{u}_\zeta \cdot \nabla \zeta + \frac{1}{2h}\sqrt{\frac{\epsilon}{Re}}\,(\boldsymbol{u}_\zeta \times \boldsymbol{k}) \cdot \nabla \zeta = -\frac{1}{2h}\sqrt{\frac{\epsilon}{Re}}\left(\frac{2}{\epsilon} + \zeta\right)\zeta + \frac{1}{Re}\nabla^2 \zeta, \tag{2.27}$$

where ∇ is the gradient operator in the (x, y) coordinates, $\boldsymbol{u}_\zeta = \nabla\psi \times \boldsymbol{k}$ is the velocity vector purely driven by the vorticity ζ, and $\boldsymbol{k}$ is a unit vector along the axis of the container rotation. This equation is actually in the same form as that derived by Zavala Sansón & van Heijst (2000). In (2.27) the Ekman pumping effect appears explicitly, namely the third term on the left-hand side (referred to as 'term I') and the first term on the right-hand side (referred to as 'term II'). The former corresponds to the advection of the vorticity normal to the streamline, ψ = constant, which is dictated by the vorticity itself. Since $\boldsymbol{u}_\zeta \times \boldsymbol{k}$ is facing toward the right-hand side viewed from the direction of $\boldsymbol{u}_\zeta$ and the fluid rotates usually in the counterclockwise (clockwise) direction for the cyclonic (anticyclonic) vortex, term I plays the role of carrying the vorticity outward for the cyclonic vortex (vorticity spreader), and vice versa for the anticyclonic vortex (vorticity squeezer). Thus, if the distribution of ζ within a vortex is such that the level of ζ decreases monotonically from the maximum value at the centre of the vortex as usual, term I causes the distribution to be flatter for the cyclone and sharper for the anticyclone.

Term II comes from the conservation of the absolute angular momentum, where the fluid's displacement is caused by the pumping or suction from the Ekman layer. If ϵ is small enough, term II is approximately linear in ζ, and its role can be considered as a vorticity decay, with the decay rate being almost the same for both cyclonic and anticyclonic vortices. However when $\epsilon = O(1)$, the situation is quite different due to the nonlinearity. For a cyclone the decay rate is larger, whereas for an anticyclone the decay rate is smaller or can even be negative.

In summary, the action of the Ekman layer causes the cyclonic vortex to decay fast and makes the vorticity distribution flatter, but it has the opposite effect on the

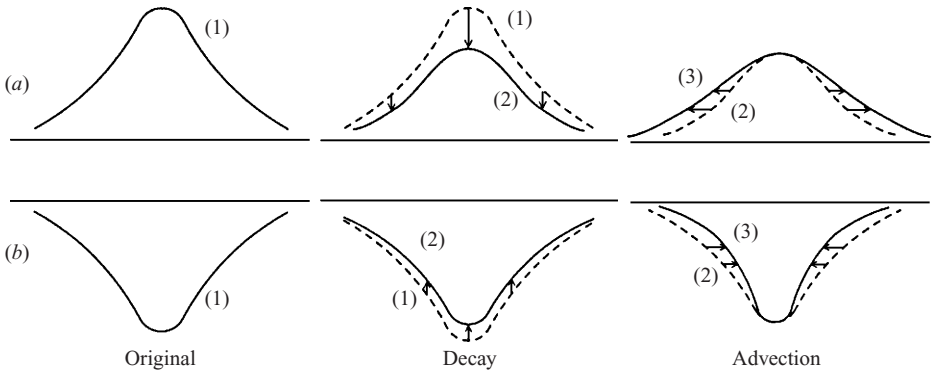

FIGURE 2. Sketch of the vorticity evolution for (*a*) the cyclonic and (*b*) anitcyclonic vortices affected by the Ekman pumping/suction.

anticyclonic vortex. Shown in figure 2 are sketches of the time evolution of vorticity distributions for the cyclones and anticyclones illustrating the concepts discussed hitherto.

2.5. *Numerical method*

The vorticity equation (2.9) is discretized spatially by centred difference with uniform $I \times J$ meshes, and the integration with respect to time is performed by using the fourth-order Runge–Kutta method. For renewal of ψ and ζ in each step of the Runge–Kutta method, (2.23*a*, *b*) are solved by using the conjugate gradient method with ILU (incomplete LU-decomposition) preconditioning. Every time (2.23*b*) is solved, its spatial average $\bar{w}/h$ is subtracted from the right-hand side; this averaged quantity should in principle be zero by (2.14) and the impermeable conditions at the lateral walls, but the accumulation of small errors turns out to cause the computation to blow up without such an adjustment.

The boundary value of ζ is given by $\zeta_w = -(\partial^2\psi/\partial n^2)_w$. For instance at the wall $y = 0$, second-order forward difference leads to

$$\zeta_w \approx -\frac{1}{2\Delta y^2}\left[8\psi_2 - \psi_3 - 6\left(\frac{\partial\psi}{\partial y}\right)_w \Delta y\right], \tag{2.28}$$

where ψ_2 and ψ_3 denote $\psi(x, \Delta y, t)$ and $\psi(x, 2\Delta y, t)$, respectively. Here, no-slip condition $u = 0$ applies, and from (2.22*a*) we can set $(\partial\psi/\partial y)_w = -(\partial\phi/\partial x)_w$.

3. Experimental method

To assist the numerical work, we performed an experiment with an open rectangular tank mounted on a turntable. The tank was made of Plexiglas with length $L = 30$ cm, width $B = 15$ cm, and height 33 cm yielding the horizontal aspect ratio $a = 2$, and filled with tap water. The water depth H was usually fixed at $H = 12$ cm corresponding to $h = 0.8$, but it was varied from 3 to 30 cm when the depth effect was considered (§ 4.5).

To provide flow visualization, we scattered polystyrene particles on the water surface. We also added blue dye to the water in order to enhance the contrast between the fluid and the particles. Roughly 1 g of liquid detergent was further added to the water to reduce the surface tension effect and to prevent the particles from becoming lumped together (van de Konijnenberg & van Heijst 1997).

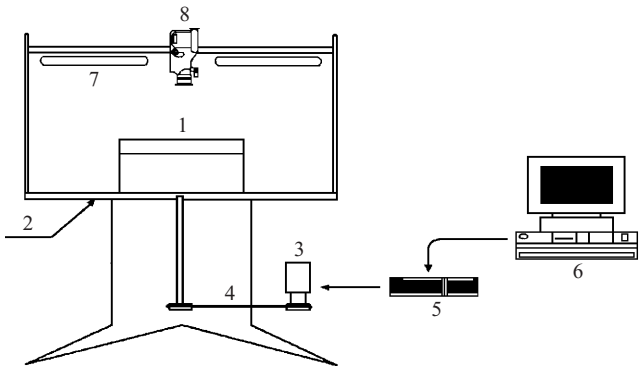

FIGURE 3. Experimental apparatus for flow visualizations: 1, rectangular tank with water; 2, rotating table; 3, servo motor; 4, timing belt; 5, servo-motor controller; 6, PC for servo-motor control; 7, fluorescent lamps; 8, video camera.

The turntable is driven by a variable-speed servo motor through a gearing mechanism (reduction ratio 80 : 1) and a timing belt (figure 3). The servo motor is controlled by a personal computer with a D/A converter.

Prior to the main experiment, the table was maintained at an angular speed Ω_s for a sufficiently long time so that the fluid remained at a solid-body rotation. Ω_s varied from 0.157 to 0.393 rad s^{-1}. Then at $t = 0$ the table speed was increased smoothly (refer to equation (2.4)) to $\Omega_f = \Omega_s/(1-\epsilon)$ and remained at this value. In this study the Rossby number ϵ was usually fixed at 0.625 except in § 4.4 where its effect is considered. The time interval T_s for this speed-up operation was set as 3.75 s, which gives $\omega = \pi/(\Delta\Omega T_s)$. Relative motions of the particles were then recorded by a video camera corotating with the table in the rate 30 frames s^{-1}. The recorded images were processed by a commercial PIV system (Thinker's EYES) to obtain velocity fields. Time interval between two frames used in the PIV processing varied from 1/30 to 5/30 s depending on $\Delta\Omega$.

4. Results

In this paper, the aspect ratio is fixed at $a = 2$, and the parametric study involves Re, h and ϵ.

4.1. *Verification of Ekman pumping models*

The two Ekman pumping models used in the numerical analysis are the linear pumping law (2.20) (hereinafter referred to as the L-model) and the one corrected by the addition of ϵw_{E1}, (2.21) (referred to as the M-model). For the purpose of comparison, we also run the code without a pumping effect (referred to as the N-model); in fact this corresponds to $h \to \infty$ (cf. (2.7)).

Shown in figure 4 is the evolution of the non-dimensional kinetic energy

$$\mathscr{E}(t) = \frac{1}{a}\int_0^1 \int_0^a (u^2 + v^2)\,\mathrm{d}x\,\mathrm{d}y \tag{4.1}$$

obtained by the experimental and numerical methods at $Re = 5890$ and 14 730. At the very beginning of the spin-up we can see an abrupt increase of $\mathscr{E}$. This starting flow is characterized by a spatially uniform but temporaly varying vorticity

$$\zeta = -2(1+f), \tag{4.2}$$

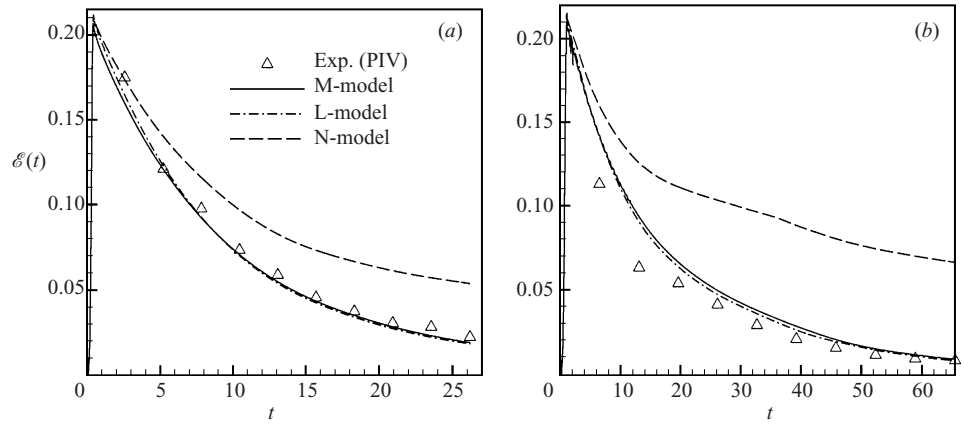

FIGURE 4. Time evolution of the kinetic energy given by the numerical and experimental methods for (*a*) $Re = 5890$ and (*b*) $Re = 14\,730$ at $\epsilon = 0.625$ and $h = 0.8$.

which comes from the equation $\partial\zeta/\partial t = -2\,\mathrm{d}f/\mathrm{d}t$ with an initial condition $\zeta = 0$ at $t = 0$; refer to Suh & van Heijst (2000) for a mathematically rigorous derivation of the starting flow equation. The graph reveals that the non-dimensional speed-up time t_s is comparatively small. Except for some critical situations, the effect of t_s on the flow evolution is in most cases negligible.

It is remarkable that the results obtained by both the L- and M-models are very close to the experimental results. Moreover the two models yield almost identical results, indicating that the contribution of the higher-order correction, (2.21), to the Ekman pumping is insignificant. On the other hand, the numerical simulation without Ekman pumping (N-model) overpredicts the experimental result considerably, and the discrepancy becomes more pronounced at higher Reynolds numbers. Several works on the axisymmetric geometry have reported that the linear Ekman pumping law predicts well the experimental (Wedemeyer 1964; Greenspan 1968; Maas 1993; Zavala Sansón & van Heijst 2000) and the numerical (Rogers & Lance 1960) results even for $\epsilon = O(1)$. Thus the present results indicate that the argument is relevant not only to axisymmetric but also to non-axisymmetric containers.

We also note that at $Re = 14\,730$ even the Ekman pumping models overpredict $\mathscr{E}(t)$, especially in the initial development. However we have found that the discrepancy becomes smaller as ϵ decreases. It would be interesting to find out what mechanism is responsible for such overprediction at high Reynolds numbers for moderate ϵ values; we conjecture that inertial oscillation in the upper layer is one of the key factors.

The reason why the higher-order correction in the pumping model brings an insignificant contribution to the upper-layer flow will now be explained. For this we express the Ekman pumping velocity w_E for $t \geqslant t_s$ as follows (see (2.17), (2.20) and (2.21)):

$$w_E = \sqrt{E}(K_0 + K_1), \tag{4.3}$$

$$K_0 = \tfrac{1}{2}\zeta, \tag{4.4a}$$

$$K_1 = K_{11} + K_{12} + K_{13} + K_{14}, \tag{4.4b}$$

$$K_{11} = -\tfrac{7}{80}\epsilon\zeta^2, \quad K_{12} = -\tfrac{3}{80}\epsilon\left(u\frac{\partial\zeta}{\partial x} + v\frac{\partial\zeta}{\partial y}\right), \tag{4.4c,d}$$

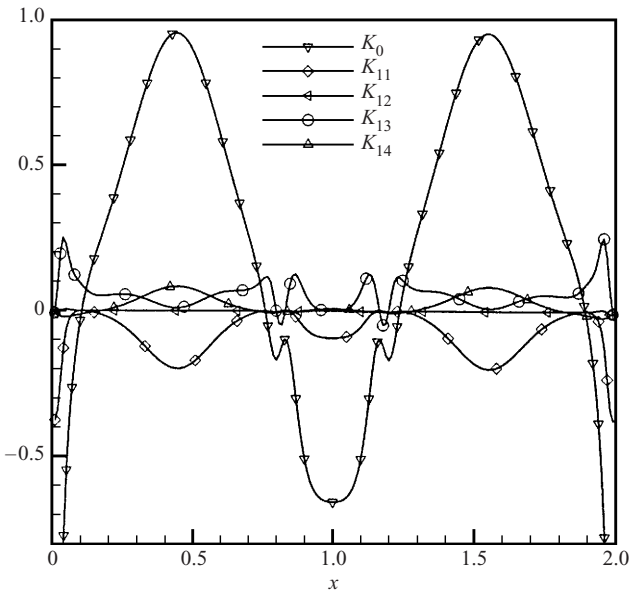

FIGURE 5. Distributions of K_0, K_1, K_{11} … K_{14} (refer to (4.3) and (4.4) in the text) at $y = 1/2$ and at $t = 32.7$; $Re = 5890$, $\epsilon = 0.625$.

$$K_{13} = -\tfrac{7}{80}\epsilon\left(-u\tfrac{\partial\zeta}{\partial y} + v\frac{\partial\zeta}{\partial x}\right), \quad K_{14} = -\tfrac{3}{20}\epsilon\left(\frac{\partial u}{\partial y}\frac{\partial v}{\partial x} - \frac{\partial u}{\partial x}\frac{\partial v}{\partial y}\right). \tag{4.4e,f}$$

Here K_0 and K_1 reflect the contributions from the leading- and first-order corrections, respectively. Figure 5 shows distributions of $K_0, K_{11}, \ldots, K_{14}$ along the centreline $y = 1/2$ obtained by the numerical simulation for the same parameter set as figure 4(*a*). It is seen that K_0 is indeed dominant. Among the four terms K_{11}, K_{12}, K_{13} and K_{14} contributing to the first-order correction (K_1), K_{11} is the largest. However K_1 is further decreased because K_{11} is partially cancelled out by the other terms. The ratio of $|K_{11}|$ and $|K_0|$ is

$$\frac{|K_{11}|}{|K_0|} = \tfrac{7}{40}\epsilon|\zeta|. \tag{4.5}$$

Therefore we may estimate that the relative importance of the first-order correction could be less than this ratio. For a typical value of $|\zeta| = 1$ at $\epsilon = 0.625$, we have $|K_{11}|/|K_0| = 0.11$. Even for the case of spin-up from rest ($\epsilon = 1$), $|K_{11}|/|K_0| = 0.175$. Thus our analysis renders further support to the assertion given by Maas (1993): '… the extra Ekman pumping term does not significantly alter the previous results (even though $\epsilon = 0.45$). This has to be attributed to the smallness of the numerical factors preceding the extra terms, …'.

Equation (4.5) also implies that the importance of the first-order correction is roughly proportional to the level of the vorticity. Since the vorticity decays with time, the relative importance of the first-order correction is further decreased with time.

Shown in figure 6 are the evolution of the velocity vector fields obtained by the experimental and numerical methods for the same parameter sets as figure 4(*a*). As implied in figure 4(*a*), the numerical results with either the L- or M-model predict well the experimental result both qualitatively and quantitatively. On the other hand,

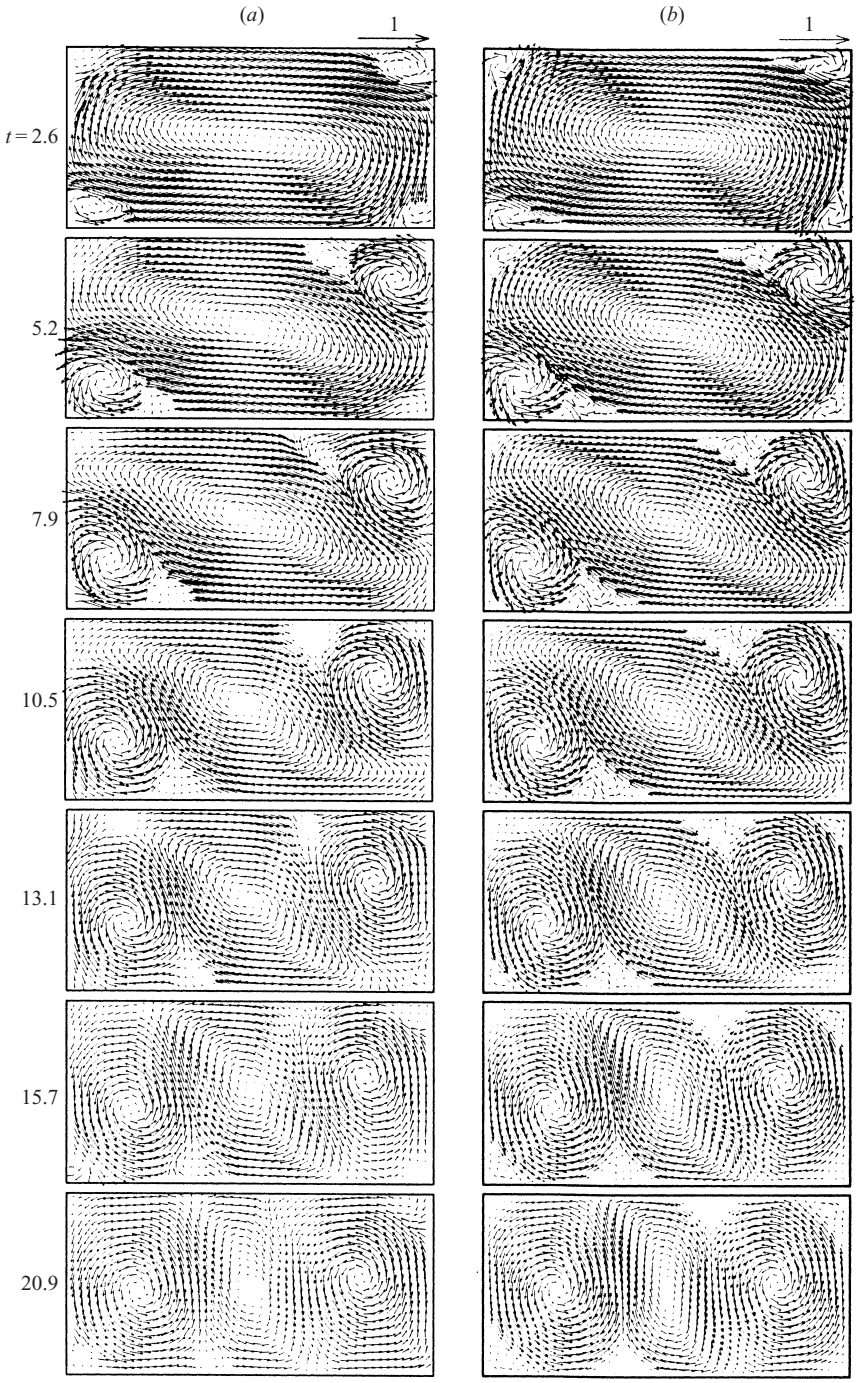

FIGURE 6 (*a*, *b*). For caption see facing page.

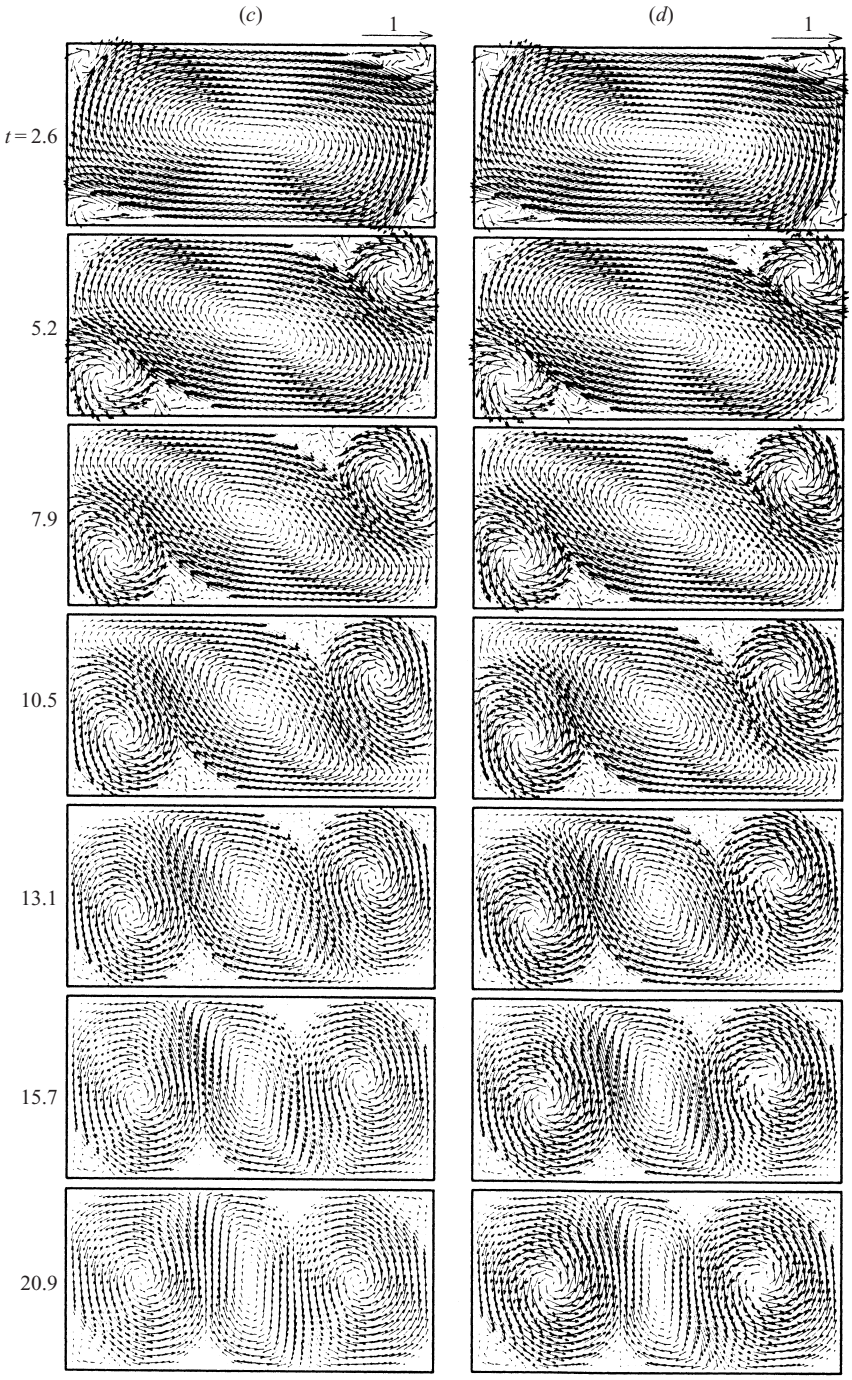

FIGURE 6. Velocity vectors at the times indicated for $Re = 5890$, $h = 0.8$, and $\epsilon = 0.625$ given by (*a*) experiment, and numerical methods with (*b*) M-, (*c*) L-, and (*d*) N-models.

the flow fields predicted by the N-model are on the whole stronger than the others, although the cell structures are in close agreement with the experiment. For this parameter set, the two cyclonic cells generated at the left-bottom and right-top corners grow with time until a stable three-cell structure is established; no merging is observed in this case (hereafter 'top' and 'bottom' walls denote the walls at $y = 0$ and 1 respectively and should not be confused with the lower wall at $z = 0$ or the free surface of the contained liquid at $z = h$).

At higher Re (figure 7), merging of the two cyclonic vortices occurs, and some discernible differences among models appear in the evolution of vortices. In the initial development up to $t = 32.5$, three models are in close agreement with the experiment except that the N-model shows overall stronger flows than the experiment. Both L- and M-models (figure 7b, c) are successful in reproducing the final three-cell structure of anticyclone–cyclone–anticyclone (hereafter referred to as pattern '$-+-$') observed in the experiment. While the L-model shows the merging occurring at an earlier time than the experiment, the M-model shows almost a perfect agreement.

On the other hand, with the N-model, the final state is characterized by a $+-+$ pattern, contrary to the other results and indicating that use of the Ekman models is essential for correct prediction of vortex interactions. The picture for the N-model also clearly demonstrates vortical flows rather stronger than the experiment, being consistent with figure 4(a).

4.2. *Typical evolution of vortical flows*

We describe typical flow evolution based on distributions of vorticity and streamlines for $h = 0.8$ and $\epsilon = 0.625$. Figure 8 shows the case of $Re = 8840$ obtained by the M-model. As with $Re = 14\,730$ (figure 7b), this case also results in cyclone merging.

Initially the anticyclone with uniform vorticity of $\zeta = -2$ occupies most of the central region ($t = 6.6$). Although the anticyclone is shrunk with time by the action of two cyclones, its vorticity level is almost unchanged. The central anticyclonic vortex on the other hand drives the boundary layers near the bottom and top walls to supply each detaching shear layer with a high level of positive vorticity. The shear layers in turn roll up around the corner cyclones to make the cells bigger, like snowballs. Rapid growing of the cyclones necessitates entrainment of fluid material of negative vorticity situated in the central anticylone; otherwise, only feeding of the thin shear layer with thickness of $O(Re^{-1/2})$ results in a cell size at most $O(Re^{-1/4})$ after an $O(1)$ time has elapsed. Typical examples of entrainment of surrounding fluid during roll-up of shear layers are flow over a wedge in a shock tube (photo number 82 in Van Dyke 1982), and vortex sheet roll-up in the Trefftz plane (Krasny 1987). Thus the pair of cyclonic vortices shows a peculiar distribution of vorticity especially near the periphery: positive and negative vorticity resides alternately. At $t = 26.0$ the anticyclone takes a dumbbell shape (van Heijst *et al.* 1990) after which it splits into two. During this process, the two cyclones merge and occupy the central region. The split anticyclones move around the merged cyclone, arrive near the left- and right-hand edges, and become stable cells. The final, almost steady-state is thus characterized by a $-+-$ pattern.

The essence of the above scenario applies for the range of Reynolds numbers accompanying the cyclone merging. At higher Reynolds numbers, however, the vortical flows are more active and two-dimensional instability also occurs. Figure 9 shows the case of $Re = 14\,730$. We can see instability in the detaching shear layers ($t = 13.1$) and subsequent folding ($t = 19.6$). It is expected that such instability may enhance mixing of fluid material in the cyclones which contain different signs of

vorticity. We also note that the growth rate of the corner cyclones is almost the same as that at $Re = 8840$, indicating that the entrainment hypothesis is indeed plausible. The overall flow evolution is also seen to be more active than the previous case.

4.3. *Effect of Reynolds number*

In the above, there has already been some discussion of the effect of Reynolds number on the flow evolutions. In this subsection further issues will be addressed. Figure 10 shows $\mathscr{E}(t)$ for four Reynolds numbers obtained by the M-model. It is seen that at a given time the kinetic energy is increased as Re increases. We have seen from figures 4(a) and 4(b) that the Ekman pumping models give rise to a higher decay rate of the kinetic energy than the N-model, implying that the Ekman pumping velocity promotes decay of the kinetic energy. Since the Ekman pumping velocity is proportional to $1/\sqrt{Re}$ (cf. (2.20) or (2.27)), the energy decay should be weaker at higher Re as shown in figure 10.

To capture the effect of Re on the detailed temporal flow evolution, the vorticity distributions along the centreline $y = 1/2$ are plotted as functions of x and t in grey scale as shown in figure 11. In this plot the extremum of positive vorticity is white while that of negative vorticity is black. Except near the side boundaries, the white thus corresponds to the cyclonic vortex and black to the anticyclonic vortex. Every plot in this figure is symmetric with respect to $x = 1$ suggesting that the corresponding flow pattern is antisymmetric.

The initial development (up to approximately $t = 25$), being independent of Re, clearly indicates shrinkage of the central anticyclone and expansion of the two cyclones. However after $t = 25$ completely different patterns appear depending on Re. For $Re = 5890$, the anticyclone is narrowest at around $t = 25$ and then expands slowly to become comparable in size to the surrounding cyclones. For the other values of Re, the initial anticyclone loses its trace at $t = 30$, which should be a symptom of the cyclones merging, and only the merged cyclone is seen for a while. Then near $x = 0.5$ and 1.5 two anticyclones emerge abruptly with the central region still occupied by the cyclone. Such an abrupt emergence of anticyclones implies that those vortices grew enough to reach the centreline $y = 1/2$ (e.g. compare the two vorticity patterns at $t = 39.3$ and 45.8 in figure 9).

From this figure we can also find that as Re is increased the shape of the boundaries between positive and negative vorticity becomes more irregular and complex. The initial irregular shape shown in the region $0.5 \leqslant x \leqslant 1.5$ for $Re = 14\,730$ (figure 11d) is caused by the instability of the shear layers (cf. the plot for $t = 13.1$ in figure 9). The irregularity occurring after $t = 46$ near $x = 0.8$ and 1.2 is due to the rotation of the central, dumbbell-shaped cyclone. Figure 12 shows four sequences of vorticity distributions related to this outcome. We can see that while the central cyclone rotates its width measured along the line $y = 1/2$ does indeed vary considerably. At low Re (figure 11b) such irregularity is not observed, indicating that neither instability of the shear layer nor the rotation of the dumbbell-shaped cyclone occur.

4.4. *Effect of Rossby number*

The Rossby number, ϵ, is contained in terms I and II in (2.27). As discussed in § 2.4, the former acts as a vortex spreader (cyclonic) or a vortex squeezer (anticyclonic). Therefore for the usual vortices (i.e. bell-shaped distribution of vorticity, figure 2), increase of ϵ yields stronger vorticity spreading or squeezing. As briefly discussed at the end of § 2.4 the role of ϵ in term II is not so simple, but depends on the magnitude

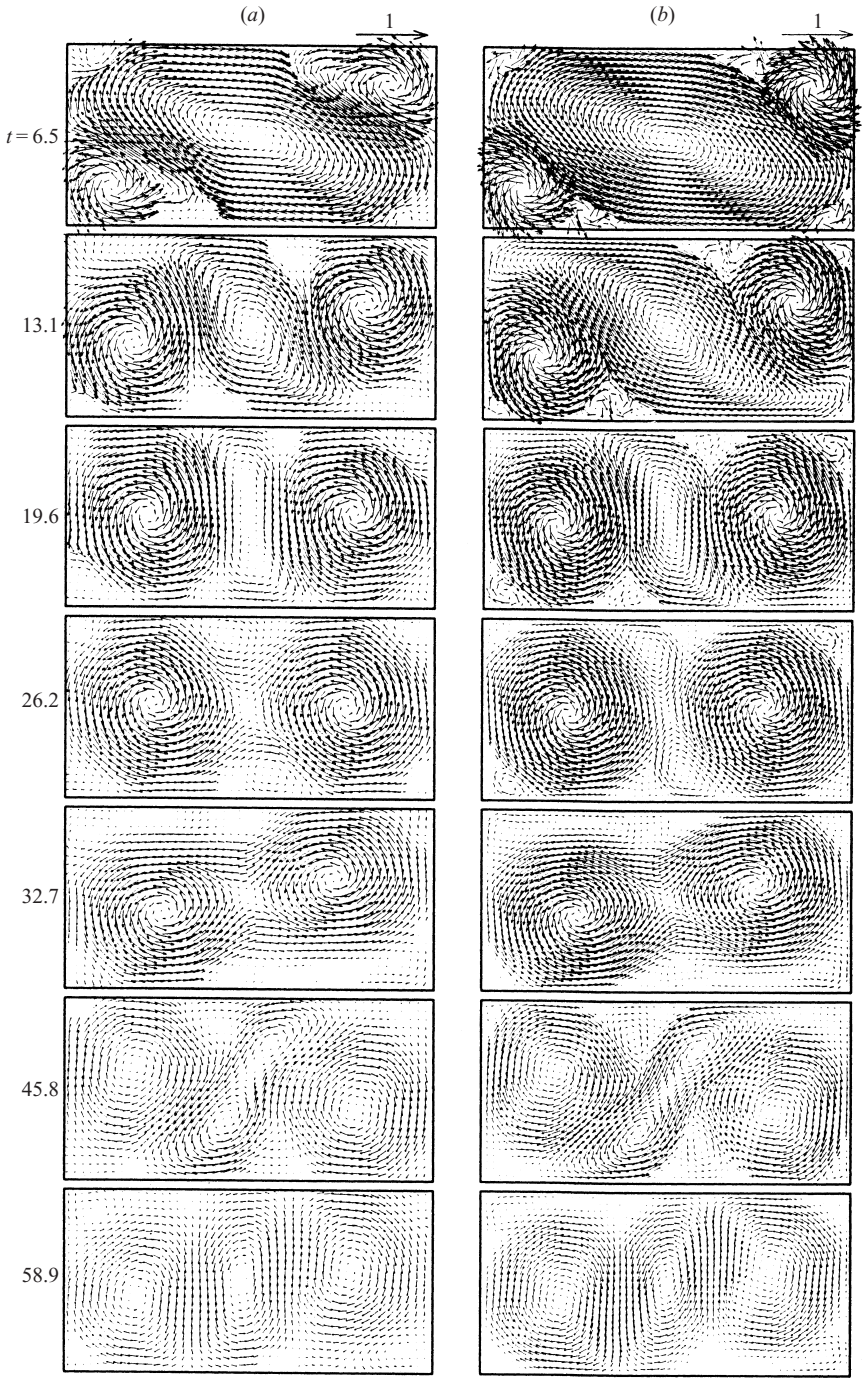

FIGURE 7 (*a*, *b*). For caption see facing page.

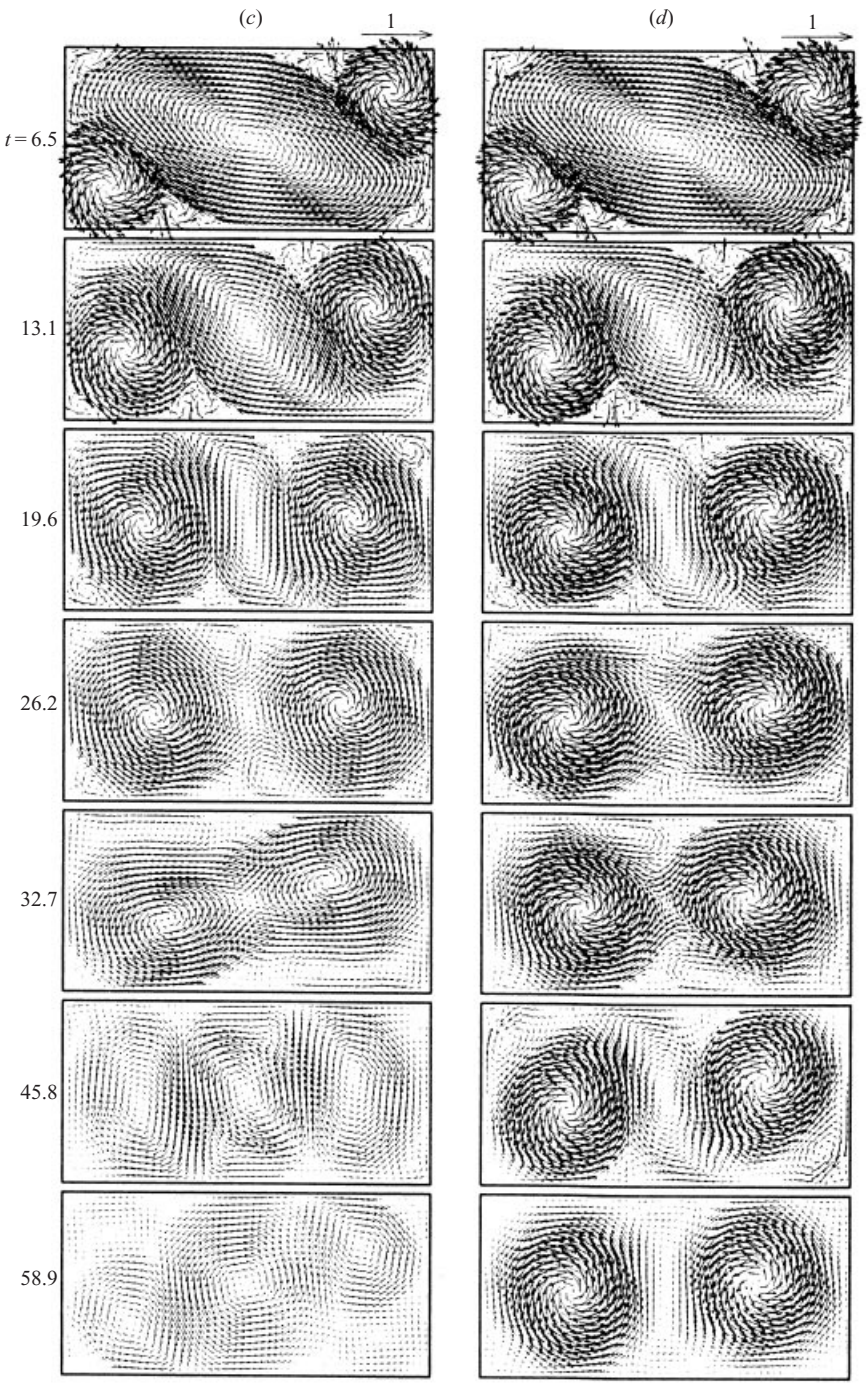

FIGURE 7. Same as figure 6 but for $Re = 14\,730$.

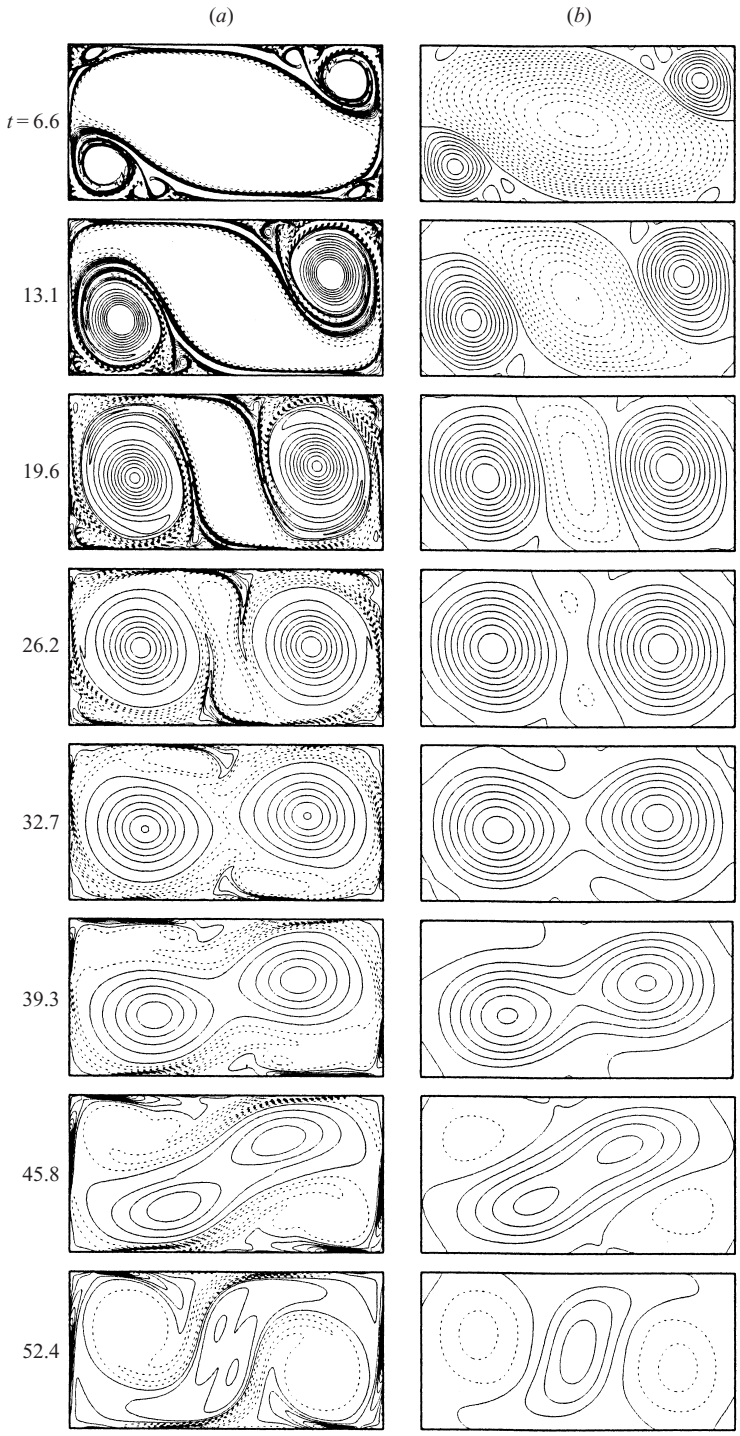

FIGURE 8. Contours of (*a*) vorticity and (*b*) streamlines at the times indicated for $Re = 8840$, $h = 0.8$, and $\epsilon = 0.625$ given by the numerical method with the M-model. Solid/dashed lines indicate positive/negative values. Intervals for the contour levels are 0.5 for the vorticity and 0.01 for the stream function.

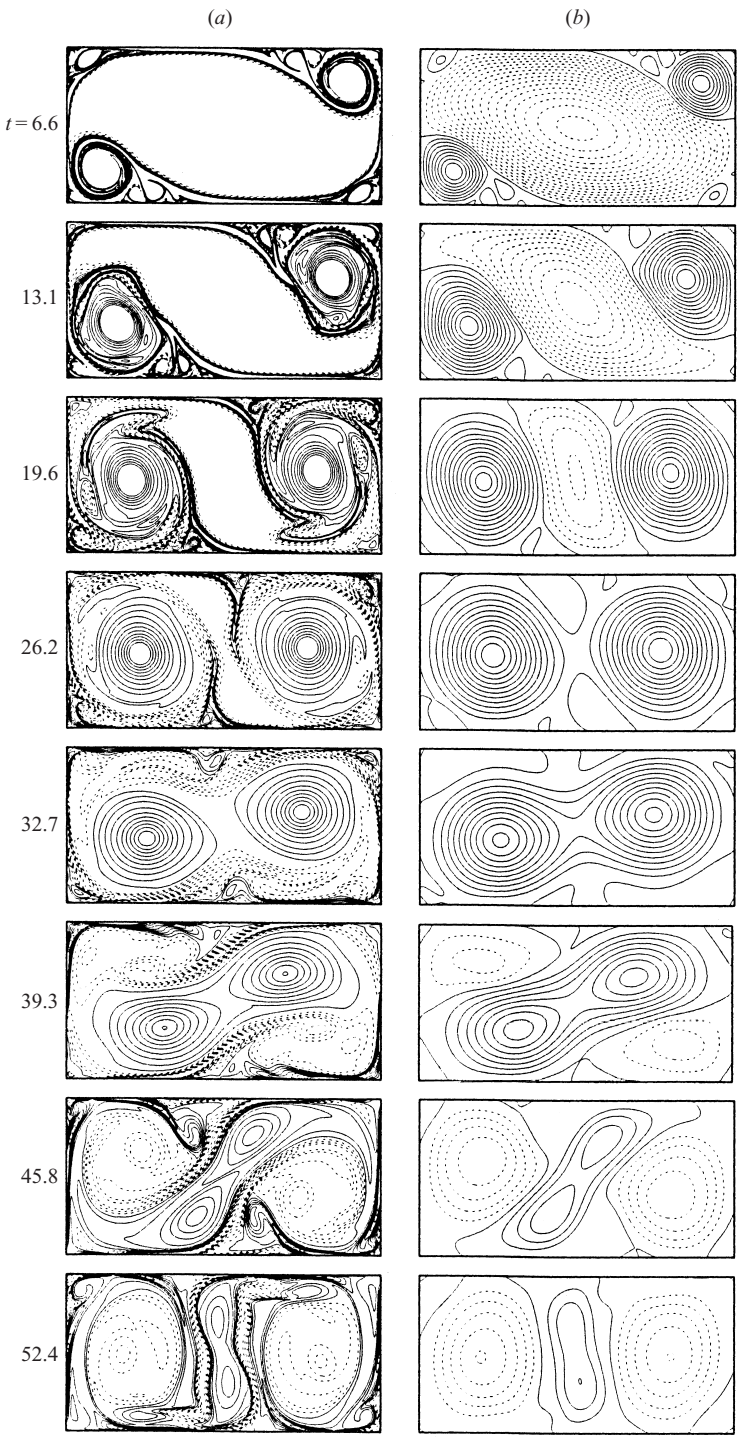

FIGURE 9. Same as figure 8 but for $Re = 14\,730$.

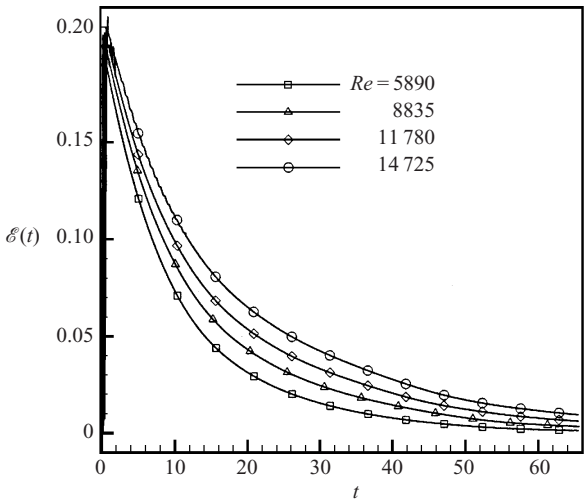

FIGURE 10. Time evolution of the kinetic energy given by the numerical methods with the M-model for $\epsilon = 0.625$ and $h = 0.8$ and various Reynolds numbers as indicated.

of ϵ and the value as well as the sign of ζ. When $|\zeta|$ is small enough, which is typical in the later stage of the spin-up process, increase of ϵ results in a smaller decay rate of ζ regardless of the rotational direction of the vortex. When ζ is of $O(1)$, which is typical in the early stage of the spin-up process, the effect of ϵ can be stated in two ways depending on the level of ϵ. If ϵ is small enough, increase of ϵ gives a smaller decay rate of ζ, and this holds for both cyclonic and anticyclonic vortices as before. If ϵ is of $O(1)$, the decay rate for the cyclone is higher than that for the anticyclone; as an extreme case when $\zeta = -2/\epsilon$, i.e. starting flow vorticity in the spin-up from rest, the decay rate becomes zero. In summary, except both for the case of $\epsilon = O(1)$ and for the starting flow, increase of ϵ is expected to give rise to a smaller decay rate of ζ. The numerical results given by the M-model, figure 13, supports our assertion.

Figures 14 and 15 compare the evolution of velocity vectors for $\epsilon = 0.32$ and 0.8. At $\epsilon = 0.32$ (figure 14) cyclone merging does not occur (experiment) or occurs very slowly (numerics), whereas at $\epsilon = 0.8$ (figure 15) merging takes place in a regular manner as in figure 7. Thus we infer that smaller ϵ makes the overall flow decay faster resulting in slower or no cyclone merging.

4.5. *Effect of liquid depth*

The effect of h on the spin-up flow evolution can be understood more simply than that of ϵ. The vorticity equation (2.27) shows that terms I and II contain h in the denominator only. Thus increase of h evidently leads to a weaker Ekman-pumping effect. The equation also reveals that h exerts the same influence as $\sqrt{Re}$ on the flow evolution as far as the inviscid motion is concerned.

Although an increase of h is simply connected to the decrease of the Ekman pumping velocity, its influence on the spin-up flows is not monotonical. Figure 16 shows the evolution of vorticity contours for four different h values at $Re = 11\,780$ and $\epsilon = 0.625$ obtained numerically. At $h = 0.2$ (figure 16*a*), the flow decays fast due to a strong damping action of the Ekman layer, and no merging of the cyclones takes place. A similar result was obtained for $h = 0.4$. At $h = 0.6$, 0.8, 1.0 and 1.2, we obtained merging of cyclones, and figure 16(*b*) shows a typical case.

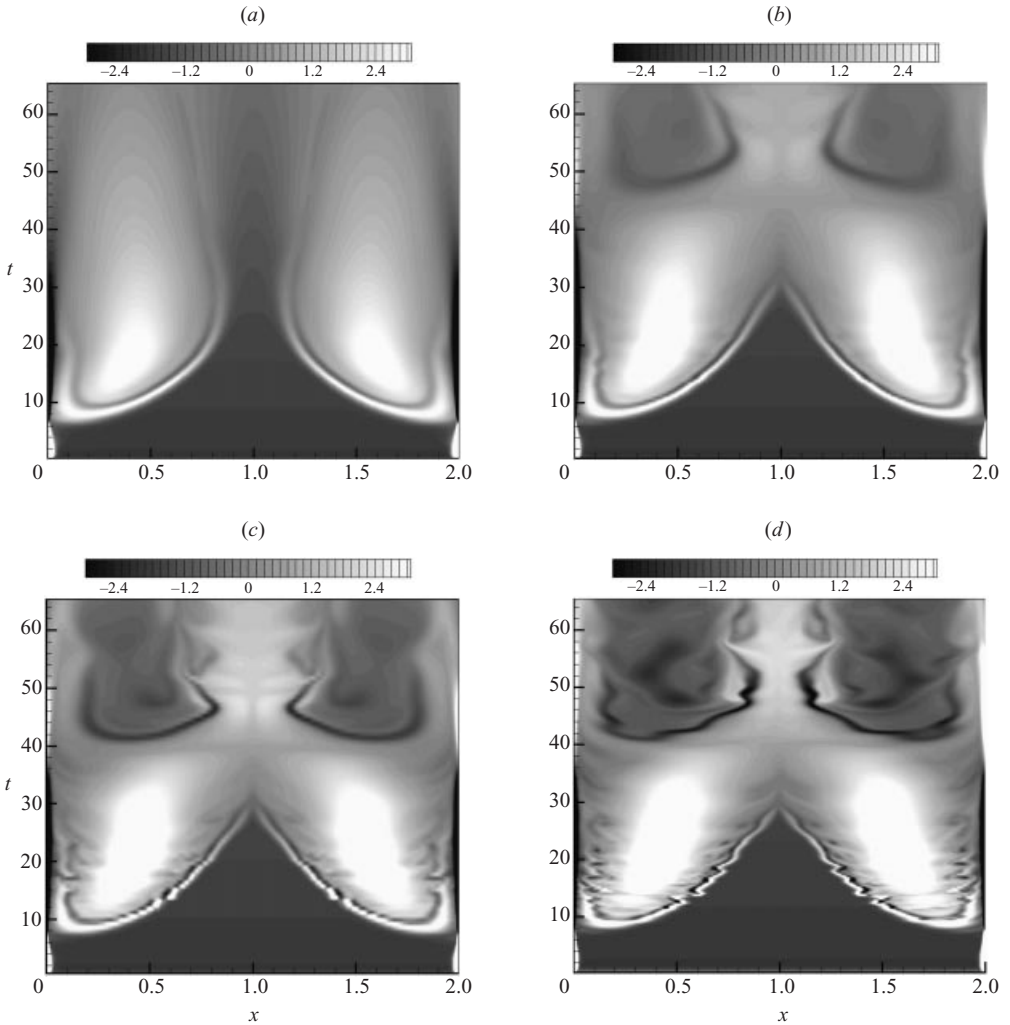

FIGURE 11. Time evolution of the vorticity distributions along the centreline $y = 1/2$ given by the numerical method with the M-model for $h = 0.8$, $\epsilon = 0.625$ and for (*a*) $Re = 5890$, (*b*) 8840, (*c*) 11 780, and (*d*) 14 730.

At $h = 1.4$ (figure 16*c*) however the evolution is more complex. The behaviour of cyclones shown in the first three frames is very similar to the corresponding ones in the merging regime, i.e. figure 16(*b*). After $t = 54$ however two cyclones do not merge but move apart from each other, $t = 72$. The reason for such splitting may be explained in terms of the vortex spreader/squeezer mechanism discussed in § 2.4. At higher h, the Ekman pumping effect is weaker and thus the cyclonic/anticyclonic vortex tends to expand/shrink less than at lower h. Indeed, two anticyclones situated near the right-bottom and left-top corners at $t = 54$ for $h = 1.4$ (figure 16*c*) are larger than the corresponding ones for $h = 0.6$ (figure 16*b*), and vice versa for two cyclones. A pair of equal-signed vortices without question tends to merge when it is enlarged, as is the case for the anticyclones at $h = 1.4$. The flow patterns for $h = 1.2$ (not shown) and $h = 1.4$ (figure 16*c*) are very similar to each other up to $t = 54$, but then diverge, arriving at a $-+-$ pattern for $h = 1.2$ and $+-+$ pattern for

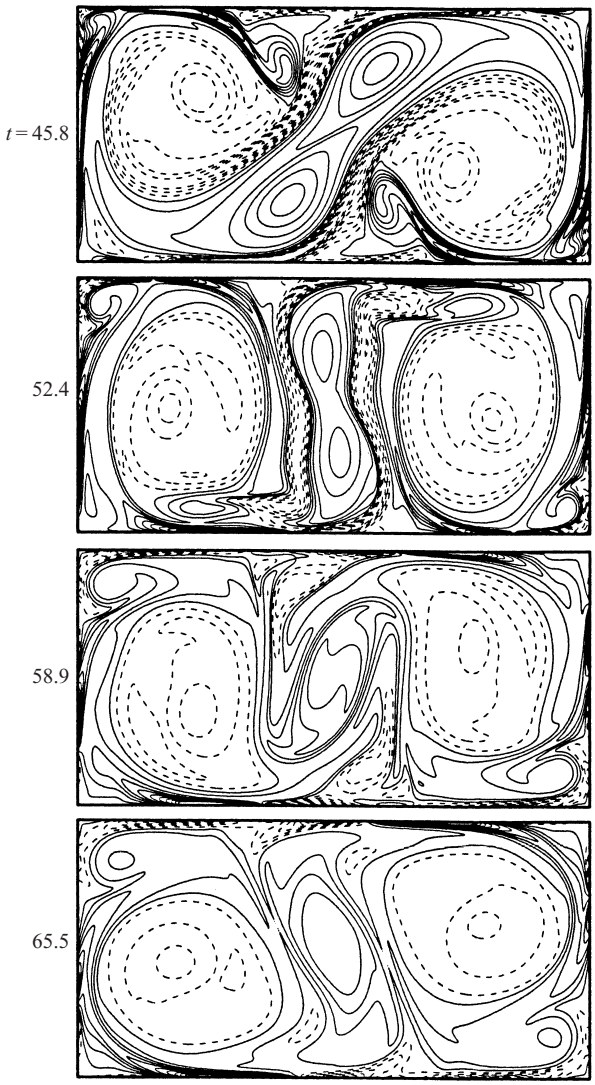

FIGURE 12. Evolution of the vorticity contours given by the numerical method with the M-model for the same parameter set as figure 11(*d*) illustrating the revolving motion of the central dumb-bell-shaped cyclonic vortex.

$h = 1.4$. Therefore a small perturbation may cause the cyclones to merge or split near $h = 1.2$–1.4; that is, we expect a critical phenomenon associated with the cyclone merging in this parameter range.

When h is slightly increased, $h = 1.6$ (figure 16*d*), the final flow pattern again differs from that of $h = 1.4$. Here too the central pair of cyclones shown as a dumbbell shape is split. However in this case each cyclone is again split into two, and the central pair is strengthened by merging with the small cyclone at the top/bottom walls induced by the anticyclones ($t = 72$). These cyclones merge in the central region and the final pattern is characterized by a $-+-$ structure ($t = 90$). We thus expect another critical situation between $h = 1.4$ and 1.6. Since the evolution patterns for $h = 1.8$, 2.0 and ∞ are similar to that for $h = 1.4$, the critical situation may also exist between $h = 1.6$ and 1.8.

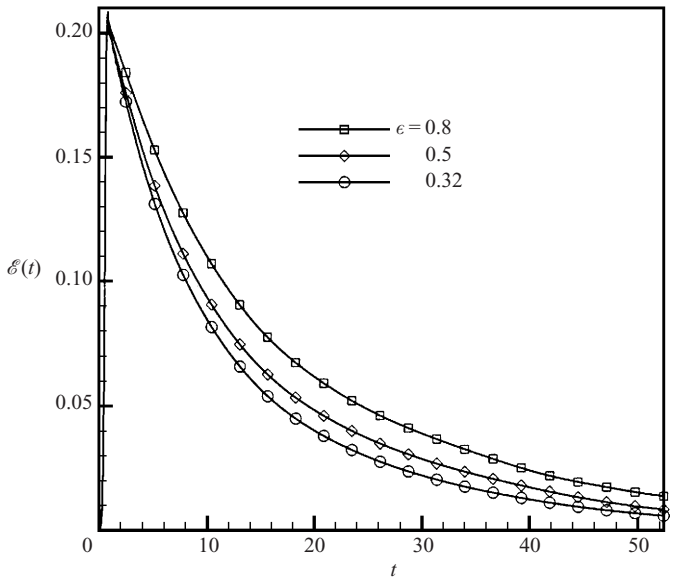

FIGURE 13. Time evolution of the kinetic energy given by the numerical methods with the M-model for $Re = 11780$, $h = 0.8$ and the three Rossby numbers shown.

4.6. *Flow regimes at* $\epsilon = 0.625$ *in the parameter space* (Re, h)*; merging event*

Up to now we have presented numerical and experimental results and discussed effects of Reynolds number, Rossby number, and liquid depth, in association with the Ekman pumping, on the overall flow evolutions in the spin-up process. In particular for $Re = 11\,780$ the depth effect was shown to be unusual as h is increased the cyclone:behaviour follows the sequence 'simple non-merging' → 'simple merging' → 'approaching but non-merging' → 'merging after a long time' → 'approaching but non-merging'. Assuming that the critical depth for such changes in behaviour should be dependent on Reynolds numbers, we fixed the Rossby number at $\epsilon = 0.625$ and changed Re and h with constant intervals to construct a parameter space (Re, h) on which to classify flow regimes associated with the cyclone merging.

Table 1 shows the results obtained both experimentally and numerically. In this table, symbol × indicates a simple non-merging (e.g. figures 6, 16*a*) and ○ a simple merging (e.g. figures 7*a*, 8, 9, 12, 16*b*). The symbol △ also indicates a cyclone non-merging event, but in this regime the cyclones initially come close and then split (figure 16*c*). In the flow regime denoted as □ the initial development is similar to that of the non-merging event △ and the cyclones first approach and then split from each other ($t = 30$, 40, 50 in figure 17). The pattern $+ - +$ created in this way is maintained for a while until two cyclones approach again ($t = 90$) and merge in the central region ($t = 100$). Figure 16(*d*) is also categorized as the regime □, but compared with figure 17 the initial approach of the cyclones is rather slow and the cyclone merging takes place early.

Overall the numerical computation predicts well the experimentally observed flow regimes. The cases in which the numerical results differ from the flow visualizations are indicated as bold symbols. The critical depths for switching from regime × to ○ at low h (hereafter denoted as h_{c1}) obtained by the numerics are slightly lower than those given by the experiment, in particular for $Re = 7360$. It shows that h_{c1} decreases with Re. The second critical depth h_{c2} (switching from ○ to △) predicted in the

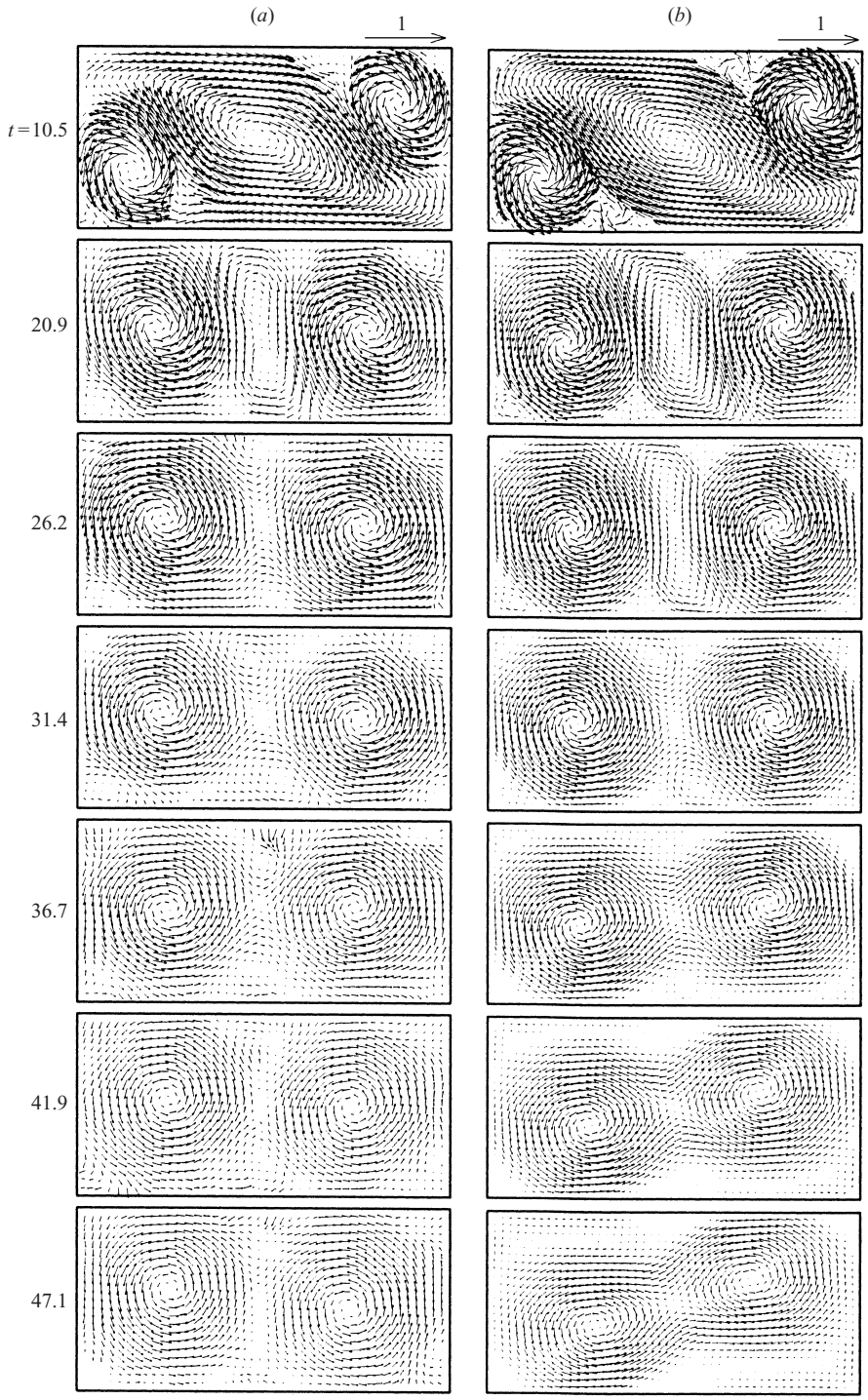

FIGURE 14. Velocity vectors at the times indicated for $Re = 11\,780$, $h = 0.8$, and $\epsilon = 0.32$ given by (a) experimental and (b) numerical methods with the M-model.

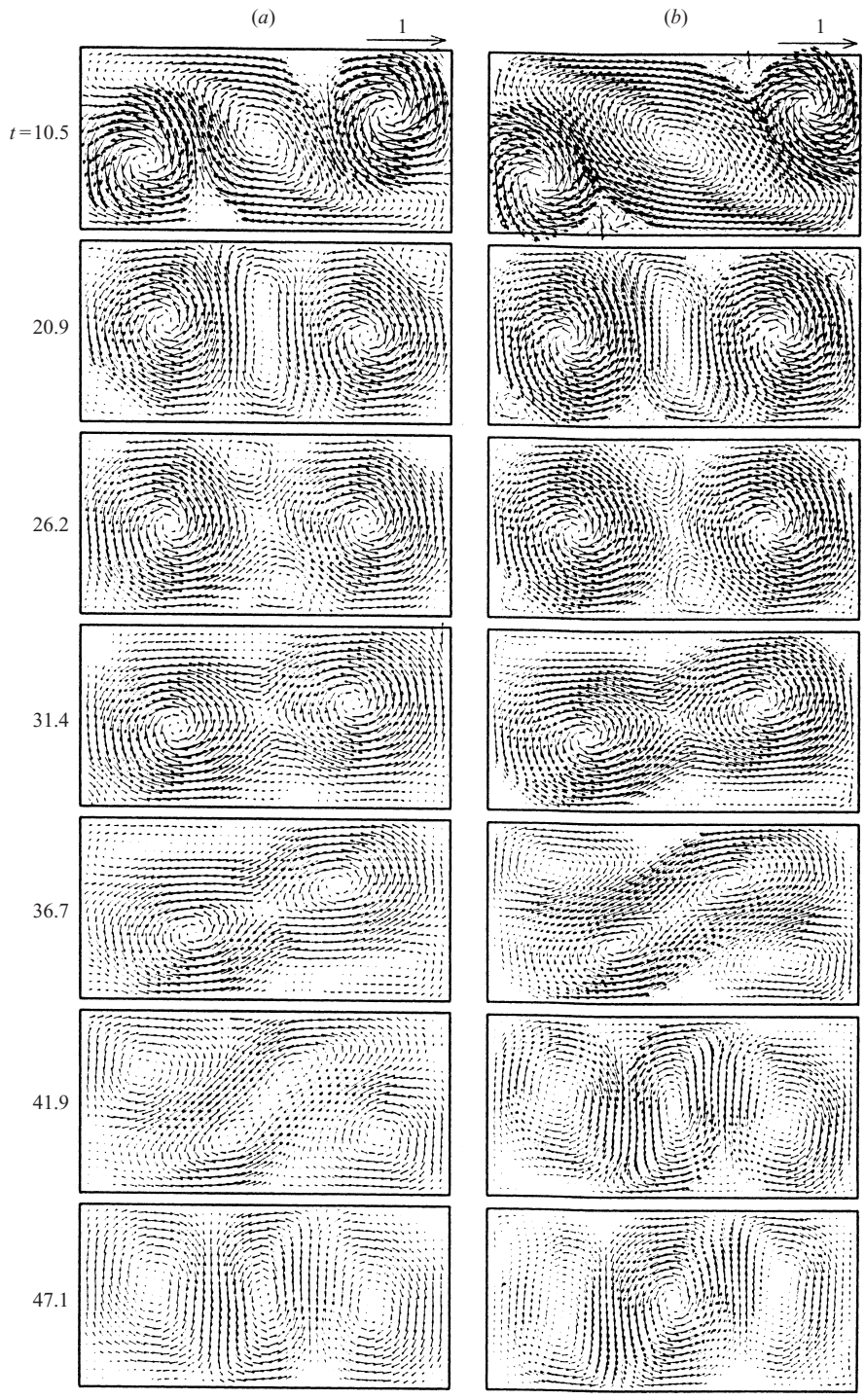

FIGURE 15. Same as figure 14 but for $\epsilon = 0.8$.

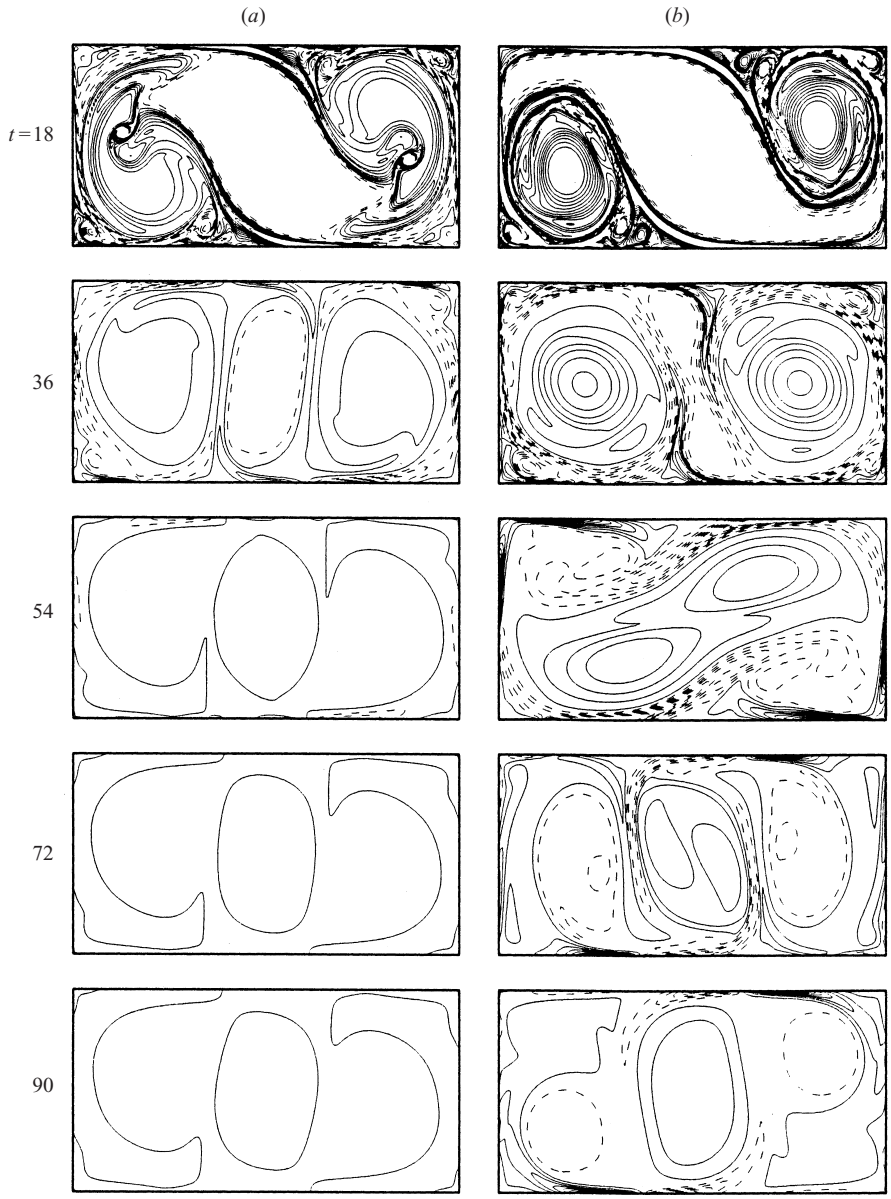

FIGURE 16 (*a*, *b*). For caption see facing page.

numerics is also slightly lower than in the experiment except for $Re = 14\,730$; h_{c2} also decreases with Re. For the third critical depth h_{c3} (switching from △ to □) however the numerical prediction shows a considerable discrepancy from the experiment, and further, the discrepancy is not consistent. For instance, at $Re = 13\,250$ the numerical value $h_{c3} = 1.4$–1.5 underpredicts the experimental value $h_{c3} = 1.8$–2.0, whereas at $Re = 14\,730$ the numerical result $h_{c3} = 1.6$–1.8 overpredicts the experimental value $h_{c3} = 1.2$–1.4.

The regime □ occurs at high h and Re, and in this parameter range the Ekman pumping is weaker resulting in a lower damping and thus more active and long-lived

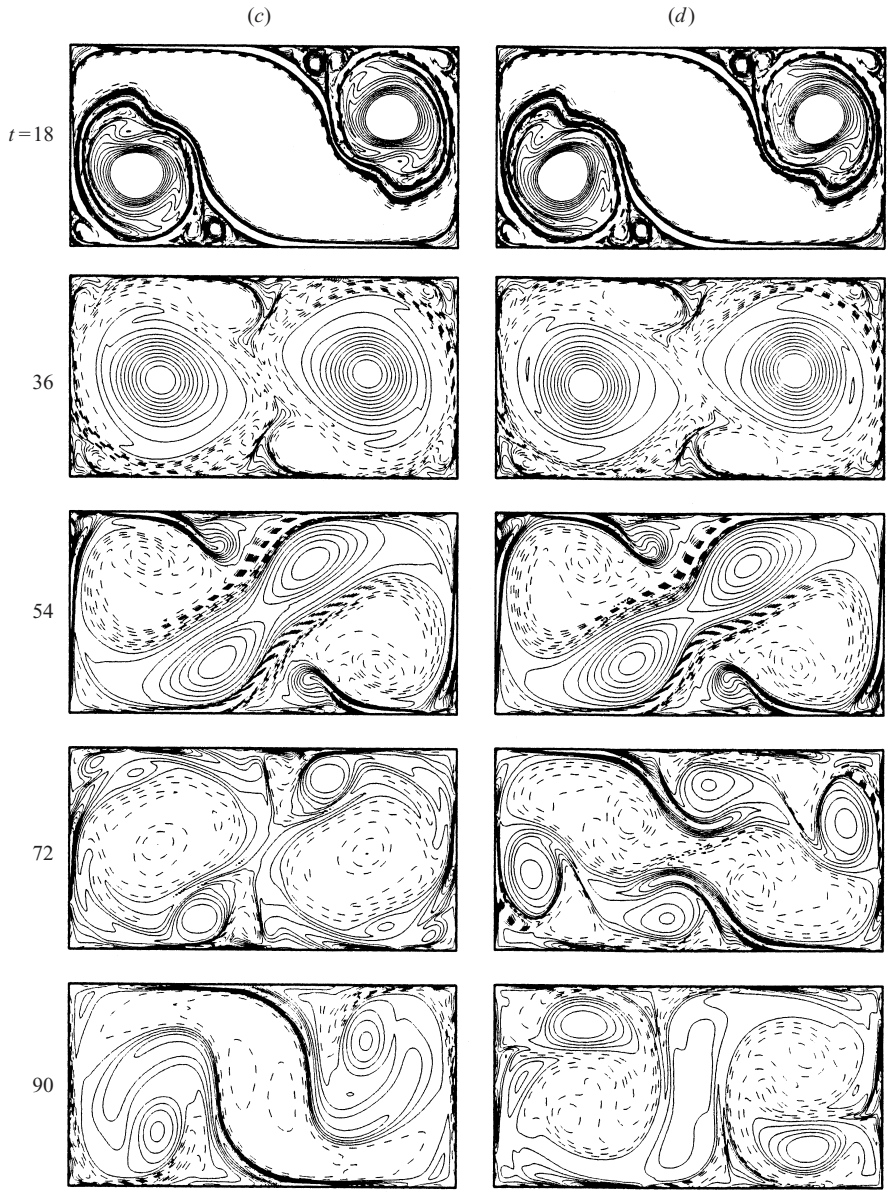

FIGURE 16. Time evolution of vorticity contours given by the numerical method with the M-model for $Re = 11\,780$, $\epsilon = 0.625$, and (*a*) $h = 0.2$, (*b*) 0.6, (*c*) 1.4, and (*d*) 1.6. Solid/dashed lines indicate positive/negative values. Interval for the contour levels is 0.5.

vortical flows. Therefore accumulation of errors caused by approximation for the Ekman pumping model should inevitably produce a discrepancy.

5. Summary and conclusions

We have been successful in fairly long-time prediction of the spin-up flows in a rectangular container by using a two-dimensional code with Ekman pumping models, and our numerical results compare well with the corresponding experimental

Re =	5890		7360		8840		10 310		11 780		13 250		14 730	
	E	M	E	M	E	M	E	M	E	M	E	M	E	M
$h = \infty$		△		□		△		△		△		△		△
2.0	×	●	○	○	○	○	△	△	△	△	□	□	□	▲
1.8	×	●	○	○	○	○	○	▲	△	△	△	△	□	□
1.6	×	×	○	○	○	○	○	○	△	■	△	■	□	▲
1.4	×	×	×	●	○	○	○	○	○	○	△	△	□	▲
1.2	×	×	×	●	○	○	○	○	○	○	△	△	△	△
1.0	×	×	×	●	○	○	○	○	○	○	○	○	△	●
0.8	×	×	×	×	○	○	○	○	○	○	○	○	○	○
0.6	×	×	×	×	×	×	×	●	○	○	○	○	○	○
0.4	×	×	×	×	×	×	×	×	×	×	×	●	×	●
0.2	×	×	×	×	×	×	×	×	×	×	×	×	×	×

TABLE 1. Regimes of cyclone merging in the parameter space (Re, h) obtained by experimental visualization (E) and the numerical method with the M-model (M) at $\epsilon = 0.625$. Here, × indicates non-merging, ○ simple merging, △ initial approaching but non-merging, □ initial approaching-splitting-merging. The shaded symbols indicate that the numerical results have a discrepancy with the experimental ones.

results. When the Ekman pumping effect is not considered (N-model), however, the numerical computation fails to provide reliable data, especially for a shallow liquid layer. Since the N-model corresponds to an infinite liquid depth and as h is increased the flow evolution undergoes several critical situations, in particular at high Reynolds numbers, it is evident that neglecting the Ekman pumping effect in a two-dimensional computation (e.g. Suh 1994 and Henderson *et al.* 1996) can lead to completely different flow patterns in the later stage of the spin-up process.

In the numerics we used both L- and M-models for the Ekman pumping effect. In most cases ($\epsilon < 0.8$), we have found that the two results are very close to each other, indicating that inclusion of higher-order terms in the Ekman pumping model is not important. The reason for this was found to be due to the smallness of the coefficients in the correction terms, and our analysis for the non-axisymmetric case is in line with that given by Maas (1993) for the axisymmetric shape. It would be interesting to do a study on the spin-down case, in which high Rossby numbers can be readily established, to see if the higher-order terms in the Ekman pumping model can improve the solutions to any extent.

We have shown that the Ekman pumping plays an important role in predicting the overall evolution of vortical flows, in particular the cyclone merging event. Two main effects caused by the Ekman pumping have been found to be damping (term II in (2.27)) and advection (term I in (2.27)). When either h or Re is small enough the Ekman pumping is significant, and the spin-up flow, due to term II, decays fast leading to non-merging. When h and Re are adjusted such that the pumping velocity is of moderate level, the Ekman pumping causes the cyclonic/anticyclonic vortices to expand/squeeze so that cyclone simple merging occurs. If h and Re are high enough so that the Ekman pumping velocity is at low level, there is no distinction between the cyclones and anticyclones, and the flow pattern tends to be more complex and asymmetric. In this regime, the vortex evolution is sensitive to a small perturbation, and a small change of h can lead to a completely different flow pattern in the final

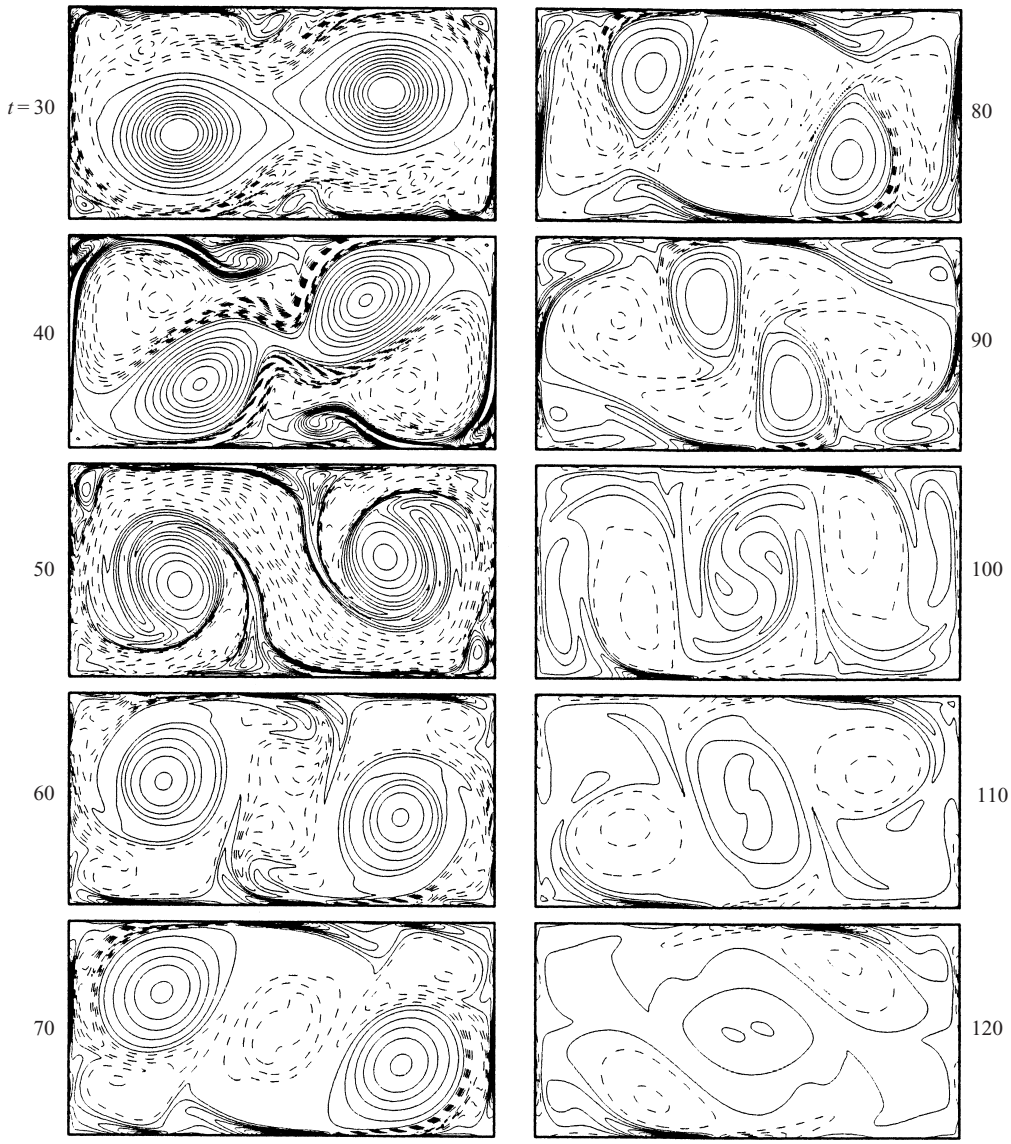

FIGURE 17. Time evolution of vorticity contours given by the numerical method with the M-model for $Re = 13\,250$, $\epsilon = 0.625$, and $h = 1.6$. Solid/dashed lines indicate positive/negative values. Interval for the contour levels is 0.5.

stage of the spin-up process (see figures 16*c* and 16*d*). Therefore predictions of the Ekman pumping models should be worse as h and/or Re is increased.

In this paper we revealed for the first time that a two-dimensional computation of the spin-up flow in a rectangular container can predict well the experimentally observed vortical flows with the use of Ekman pumping models at moderate values of h and Re. Further study is needed to enlarge the parametric space for good prediction. To improve the model, we must consider the region close to the sidewalls. In this region the vorticity is at high level and thus the induced pumping velocity is large (cf. (2.20)). However this vertical momentum cannot penetrate far into the upper layer because of the sidewall friction effect. The models proposed in this paper are

therefore liable to overpredict the Ekman pumping effects near the sidewalls. The free shear layers having high gradient of vorticity, observable e.g. in the periphery of the cyclonic vortices, also deserve our attention. It is expected that this region is susceptible to centrifugal and barotropic instability (Orlandi & Carnevale 1999) and subsequent inertial oscillations. When such three-dimensional effects are important, horizontal transport of vorticity may be enhanced. Turbulence unavoidably occurring at least in the Ekman boundary layers at higher Reynolds numbers may also cause the Ekman pumping velocity to be significantly larger. Considering these factors in developing new models for the Ekman pumping effect may be important in prediction of large-scale flows, such as oceanic flows.

This work was supported by grant No. 2000-1-30400-002-3 from the Basic Research Program of the Korea Science & Engineering Foundation. Y.K.S. also would like to thank Professor van Heijst for his invaluable help in building our turntable by providing us with detailed drawings, as well as reading this manuscript. Appreciation also should be given to Professor Duffy for his careful reading of the manuscript.

REFERENCES

Greenspan, H. P. 1968 *The Theory of Rotating Fluids*. Cambridge University Press.

Hart, J. E. 1995 Nonlinear Ekman suction and ageostrophic effects in rapidly rotating flows. *Geophys. Astrophys. Fluid Dyn.* **79**, 201–222.

Hart, J. E. 2000 A note on nonlinear correction to the Ekman layer pumping velocity. *Phys. Fluids* **12**, 131–135.

van Heijst, G. J. F. 1989 Spin-up phenomena in non-axisymmetric containers. *J. Fluid Mech.* **206**, 171–191.

van Heijst, G. J. F., Davies, P. A. & Davis, R. G. 1990 Spin-up in a rectangular container. *Phys. Fluids* A **2**, 150–159.

Henderson, D. M., Lopez, J. M. & Stewart, D. L. 1996 Vortex evolution in non-axisymmetric impulsive spin-up from rest. *J. Fluid Mech.* **324**, 109–134.

van de Konijnenberg, J. A. & van Heijst, G. J. F. 1997 Free-surface effects on spin-up in a rectangular tank. *J. Fluid Mech.* **334**, 189–210.

Kransy, R. 1987 Computation of vortex sheet roll-up in the Tresstz plane. *J. Fluid Mech.* **184**, 123–155.

Maas, L. R. M. 1993 Nonlinear and free-surface effects on the spin-down of barotropic axisymmetric vortices. *J. Fluid Mech.* **246**, 117–141.

Orlandi, P. & Carnevale, G. F. 1999 Evolution of isolated vortices in a rotating fluid of finite depth. *J. Fluid Mech.* **381**, 239–269.

Rogers, M. H. & Lance, G. N. 1960 The rotationally symmetric flow of a viscous fluid in the presence of an infinite rotating disk. *J. Fluid Mech.* **7**, 617–631.

Suh, Y. K. 1994 Numerical study on two-dimensional spin-up in a rectangle. *Phys. Fluids* **6**, 2333–2344.

Suh, Y. K. & van Heijst, G. J. F. 2000 Spin-up in a rectangular container with an internal cylindrical obstacle. *Phys. Fluids* **12**, 1986–1996.

Van Dyke, M. 1982 *An album of fluid motion*. The Parabolic Press, Stanford, California.

Wedemeyer, E. H. 1964 The unsteady flow within a spinning cylinder. *J. Fluid Mech.* **20**, 383–399.

Zavala Sansón, L. & van Heijst, G. J. F. 2000 Nonlinear Ekman effects in rotating barotropic flows. *J. Fluid Mech.* **412**, 75–91.